Physical and Genetic Mechanisms Guiding the Evolution and Development of Dendritic, Flapping Insect-Wings

Final Report
AFOSR Grant FA9550-07-01-0036

Marcelo H. Kobayashi (PI)
University of Hawaii at Manoa
Department of Mechanical Engineering
2540 Dole Street – Holmes Hall 302
96822 Honolulu, HI
and
Marguerite A. Butler (Co-PI)
University of Hawaii at Manoa
Department of Zoology
Snyder Hall 405
96822 Honolulu, HI

April 12, 2010

§1. OBJECTIVES

The primary goal of the project was the development and proof of concept of a biologically inspired topology optimization method for aerospace design.

§2. ACCOMPLISHMENTS

The objective set forth for this project has been fully attained. Indeed, the biologically inspired design methodology developed in this project, hereafter named

REPORT DOCUMENTATION PAGE

Form Approved
OMB No. 0704-0188

PLEASE DO NOT RETURN YOUR FORM TO THE ABOVE ORGANIZATION.

1. REPORT DATE *(DD-MM-YYYY)*	2. REPORT TYPE	3. DATES COVERED *(From - To)*
07-04-2010	Final	Dec 2006 - Nov 2009

4. TITLE AND SUBTITLE
Physical and Genetic Mechanisms Guiding the Evolution and Development of Dendritic, Flapping Insect-Wings

5a. CONTRACT NUMBER

5b. GRANT NUMBER
AFOSR Grant FA9550-07-01-0036

5c. PROGRAM ELEMENT NUMBER

6. AUTHOR(S)
Marcelo H. Kobayashi, P.I.

5d. PROJECT NUMBER

5e. TASK NUMBER

5f. WORK UNIT NUMBER

7. PERFORMING ORGANIZATION NAME(S) AND ADDRESS(ES)
University of Hawaii at Manoa

8. PERFORMING ORGANIZATION REPORT NUMBER

9. SPONSORING/MONITORING AGENCY NAME(S) AND ADDRESS(ES)
AFOSR
875 N RANDOLPH ST
ARLINGTON, VA 22203

10. SPONSOR/MONITOR'S ACRONYM(S)

11. SPONSOR/MONITOR'S REPORT NUMBER(S)
AFRL-SR-AR-TR-10-0254

12. DISTRIBUTION/AVAILABILITY STATEMENT

Distribution A: Approved for Public Release

13. SUPPLEMENTARY NOTES

14. ABSTRACT

The project concerned the development of a novel design methodology for structural mechanics. The developed design methodology was inspired by the EvoDevo processes in biological evolution. Thus the methodology uses a cellular division process or branch growth model to define the development of the topology of the structure. With the topology in place, a physico-mathematical model is used to determine the fitness of the design generated by the developmental process. Then an evolutionary algorithm evolves the set of rules defining the development of the structure topology, and therefore the topology itself. The methodology developed, called bioTOM, has been assessed in a number of test cases, ranging from classic benchmark problems, to realistic design problems. From the solutions obtained in these studies, it can be concluded that bioTOM provides a significant improvement, both in efficience and design performance, when compared with existing methodologies, including gradient based methods or evolutionary algorithms for topology optimization of structure topology.

15. SUBJECT TERMS
Topology optimization, evolutionary algorithms, EvoDevo, structural design

16. SECURITY CLASSIFICATION OF:			17. LIMITATION OF ABSTRACT	18. NUMBER OF PAGES	19a. NAME OF RESPONSIBLE PERSON
a. REPORT	b. ABSTRACT	c. THIS PAGE			19b. TELEPHONE NUMBER *(Include area code)*
Unclassified	Unclassified	Unclassified			

Reset

bioTOM, has been thoroughly assessed through a large number of test cases. The test cases ranged from classical benchmark problems in topology optimization to realistic engineering problems. These test cases proved the concept and showed the well-suitability of bioTOM for aerospace design.

Next in this section, a brief account of the developed design methodology is presented. This is followed by a summary of the test cases studied in this project. The section ends with the main findings of the research.

1. bioTOM

As Richard Dawkins pithily puts it "Life is the execution of programs written using a small digital alphabet in a single, universal machine language" [1]. The programs that indirectly determines the entire developmental process of living organisms are encapsulated in our DNAs. And the latter are evolved according to Darwin's laws of natural selection. Exploiting this genetic-evolutionary model for engineering is the novel paradigm set forth in this work.

This sub-section starts with an outline of the elements of map L systems that are relevant to the present work. The reader interested in the general theory of map L systems may refer to [2] and the references in that book.

At the end of 1960's, the eminent biologist Aristid Lindenmayer introduced a novel type of grammar system, where the rewriting was carried out in parallel [3, 4], rather than the sequential substitution in previous formal languages [5]. The parallel rewriting system, thereafter named Lindemayer system (or L system for short), was initially proposed to model the development of the branched topology in plants. Over the years, however, L systems became an important scientific theory in itself [2], with multiple ramifications ranging from the original model for plant development, to the mathematics of formal languages, to computer graphics, to music. Map L systems [2, 6, 7] extend the parallel rewriting in L systems to planar graphs with cycles, called maps [8]. The maps are developed according to cellular division rules that have originally been devised to model the cellular division process in simple organisms.

Formally, a map is defined as a finite set of regions. Each region is bounded by a sequence of edges and the edges intersect at vertices. Every edge is part of the boundary of a region and the regions are simply connected. These maps are analogous to cellular layers, where the regions represent the cells and the edges their walls. To develop these maps, the Binary Propagating Map 0L-systems with markers or mBPM0L-systems proposed by Nakamura, Lindenmayer and Aizawa [2, 7] is selected—mBPM0L-systems are more powerful than similar context-free map L systems [2]. The method is called binary because during the cell division

the cells divide in two. It is propagating since cells cannot fuse or vanish. The designation 0L systems refers to context-free parallel rewriting systems that do not allow for region interactions. Finally, markers specify juncture points at the edges where the cell can divide—the markers are analogous to attachment sites for division walls during mitosis [2].

Mathematically, mBPMOL-systems consist of an alphabet Σ, an axiom ω and a finite set of rules P. The alphabet is a finite, non-empty set Σ, whose elements are called letters or tokens. An alphabet can, in general, contain any symbol as letters. A simple example of an alphabet would be $\Sigma = \{A, B, C, ..., [,], +, -\}$. An axiom is a non-empty word of letters from the alphabet. The number of letters in the word should be equal to the number of edges in the initial map. For example, using the previous alphabet and for an initial map of four edges, $\omega = AABC$ is an axiom. Each rule is of the form $A \rightarrow \alpha$, where the edge $A \in \Sigma$ is called the predecessor, and the string α, composed of symbols from Σ including special symbols [,], + and $-$, is called the successor. Using again the previous alphabet, an instance of a rule would be $B \rightarrow A[-C]$. So, when rewriting a word, every occurrence of the letter B would be replaced by $A[-C]$.

The symbols [and] specify makers for possible cell-dividing walls. Symbols outside of the square brackets specify the number and type of edge subdivisions—each subdivision with the same length. Inside the brackets the first symbol is either + or $-$, placing the marker to the left or to the right of the predecessor edge, respectively. The second symbol within brackets is always a letter. The letters can carry an arrow over them to represent the local edge orientation of the successor edges relative to the predecessor edge. An example of a rule with orientation is: $\vec{A} \rightarrow \vec{B}\overleftarrow{A}[-\vec{C}]x$.

The cell division process is effected in the derivation phase, where each cell is scanned searching for matching markers. If in a cell there exist two markers in different edges, and both markers carry the same letter and follow along the same orientation, then, depending on division criterions explained below, a cell division can be formed connecting these two markers. More than one pair of matching markers can be found in one cell, however. In this case, and owing to the binary character of the method, only one pair of markers is selected for connection and the remaining markers are discarded.

The selection and validation of the edge pair is performed according to two cell division criterions: (1) the angles in the divided cells must be larger than a prescribed lower limit; (2) the areas of the offspring cells must be larger than a predefined percentage of the parent cell. The first criterion prevents the creation of cells with too narrow wedges angles, while the second precludes excessively slender

or relatively minute offspring cells to form. When multiple markers are available, the first pair to pass the two criterions above are selected and the rest are dropped.

The cellular division process explained above is best grasped with an example. Consider, for instance, the alphabet $\Sigma = \{A, B, x, [,], +, -\}$, the initial map or axiom $\omega = ABAB$ and the production rules:

$$\begin{aligned} A &\rightarrow B[-A]x[+A]B \\ B &\rightarrow A \end{aligned}$$

The symbols for which a rule is assigned—A and B in this example—are called non-terminal tokens, whereas the remaining symbols are called terminal tokens. The rules for these latter tokens are not listed because these tokens are constants; for instance, a symbol x in a word is copied as x in the rewriting.

The derivation process starts with each edge of the initial map being assigned a label—see figure 1 top—and a global orientation that defines the left (+) and right (-) branching—the orientation is counter-clockwise in this example. Then each edge is relabeled and divided according to the corresponding rule. Thus, in this example, the edges labeled B are relabeled A and no sub-division takes place. The edges labeled A are sub-divided into three new and equal segments. Consider, for example, the edge A at the bottom. The first segment is labeled B, the second x and the third again B. After the first segment, a marker A ought to be attached to the right (the symbol $-$ precedes the marker A within the first parenthesis), but since the marker would lay outside of the map this action is voided. Moving along the edge according to the global orientation, at end of the second edge x, a marker A is placed at the left of the edge. Applying this rewriting process for the remaining A, two markers are obtained, labeled A pointing to inside the initial map. Both markers are of the same type and assuming the two aforementioned criterions are satisfied the cell is divided by connecting the attachment sites of each edge. The result is the new map in figure 1—first step. Iterating this cell division process generates a sequence of maps that models the developmental stages of the structural topology.

Remark 1. *Note that the cell division would stop if, at a certain stage, all edges were labeled with a terminal token. However, stopping only when all letters are terminal tokens could lead to infinite iterations: for example, if x would be absent from the previous rules. Thus a maximum number of cell divisions is specified and the actual number of developmental stages for the topology generation is optimized in the evolutionary algorithm.*

Remark 2. *The cellular division process described above corresponds to the original map L systems by Nakamura and Lindenmayer and Aizawa [2, 6, 7]. Here it is modified slightly to allow for variations of properties, such as edge radius, within the topology. The approach is analogous to changing the state in a turtle interpretation of L systems [2] and essentially it provides a way to modify the characteristics of the structure with rules. So, terminal tokens are introduced that, when present in a rule, will change, by a quantum amount, some specific properties of the topology. For example, the symbols * and / specify the change of the radius of the edge by a quantum ratio* δ_r*. So the first rule in the previous example could now include these symbols as:* $A \rightarrow *B[-*A]/x[+*A]B$*. With this new rule, at the second developmental stage would lead to the map:* $\omega_2 = *A[-**B[-*A]/x[+*A]B]/x[+**B[-*A]/x[+*A]B]A*B[-*A]/x[+*A]B*A[**B[-*A]/x[+*A]B]/x[+**B[-*A]/x[+*A]B]A*B[-*A]/x[+*A]B$ *and the first edge A would have a radius* $\delta_r * r_0$ *where* r_0 *is an initial radius, the first edge B would have a radius* $\delta_r^2 * r_0$ *and so on. In this way, it is allowed the control of the edge radius along with the developmental stages. Introducing more tokens of this type allows the control of any desired design variable.*

Remark 3. *As explained in [2], the cellular division in living organisms entail two stages: a division stage proper and a cellular dynamic stage. So after each cellular division, actual cells deform according to forces acting on their walls. Because structural topology is the only interest, this dynamic stage is modeled as Picard iterations for the equilibrium of two forces acting on the map vertices: an elastic, spring force on each edge of the topology and an "osmotic" pressure proportional to the inverse of the area of each region. The elasticity constant of each edge and the osmotic pressure constant are modified, and can, therefore, be evolved within the topology, using the state rules explained in the previous remark. Also, to increase the efficiency of the overall methodology, the maximum number of Picard iterations is bounded to a small number.*

Remark 4. *The original map L systems deals with convex regions only [2, 6, 7]. In this work, topology optimization is performed with regions that can be non-convex. So to extend map L systems for maps with non-convex regions, a third criterion is added for cellular division, where it is required the new edge dividing the parent cell to remain inside the parent cell.*

At the end of the division stages, a planar topology is defined. With this topology, a finite element (FE) model can be formulated to calculate the fitness of each design—the details of the FE model for each test case are explained below. The fitness of each design can then be evolved using an evolutionary algorithm.

Evolutionary algorithms [9, 10] are biological metaphors that produce high quality designs by identifying, recombining and enhancing the best features present in an adapting pool of replicators. Before the genetic encoding is explained, recall the basic elements of evolutionary algorithms. In these algorithms, the evolution starts with a population of individuals, each of which carrying a genotypic and a phenotypic content. The genotype encodes the primitive parameters that indirectly determine an individual layout in the population. Here they consist of the parameters defining the map L system and the geometry and physical properties of the object. The phenotype relates to the ensuing structural model: its topology, geometry and physical properties. With the phenotype, the evaluation of the fitness of each individual design is obtained using a physico-mathematcal model and the finite element method. The fitness will vary from problem to problem, and in the case of multi-objective optimization multiple functions are evaluated for each individual. The evolutionary algorithm then advances the current population to the next generation by applying selection, mutation and crossover operators.

Genome definition. Fixing an alphabet Σ, there are three classes of parameters that affect the topology defined by the map L system in our variant of the mBPMOL-system. The first is the axiom word ω, which has an effect on the growth and dynamics of the developmental stages. The axiom is encoded as a word defined by the same letters of Σ. The second class are the edge production rules P. In keeping with the analogy with biological systems, the production rules may be seen as the regulators that control the complex processes involved in the production of cells, organs, limbs, etc. by parallel interpreting the DNA. Each production rule of the map L system is encoded according to a master rule of the form:

$$Y \to X_1 X_2 \dots X_{n-1} X_n$$

where Y is a non-teminal token and X_i denotes terminal, non-terminal or special tokens. The number of slots in the rules, n, is decided by the user and is the same for all rules—to avoid bracket mismatches, if X_i includes a bracket $X_i = [\pm A_i]$ is defined with A_i a terminal token or the non-terminal token x. Finally, the remaining genome is filled in with parameters defining the geometry or physical properties of the object such as initial edge thickness or initial edge spring stiffness modulus.

In summary, the genome can be seem as a partitioned ribbon whose first part is occupied by the letters of axiom, the second by the production rules and the third by geometric and physical parameters pertinent to the body.

Multi-objective optimization In multi-objective optimization problems, there

is a considerable number of candidate metrics for defining optimality. In the present work, the most commonly adopted criterion of Pareto optimum is chosen (see, for instance, [11]) as explained below.

The optimization problem can be stated as follows: Find the minimum of

$$\{f_1(x), \ldots, f_n(x)\},$$

subject to

$$g(x) \leq 0,$$

where x is the vector of design variables, f_i is the *i-th* target or objective function and g is the constraint vector. In the present work, constraints are enforced through penalization of the fitness values. A vector satisfying the constraint is called feasible. A feasible vector ξ is Pareto optimal or nondominated if there is no feasible vector x in a neighborhood of ξ such

$$f_i(x) \leq f_i(\xi)$$

for all $i = 1, \ldots, n$ and for at least one $i \in \{1, \ldots, n\}$

$$f_i(x) < f_i(\xi).$$

Hence a Pareto optimum is a point where around it you cannot measurably improve some targets, without simultaneously worsening others. The set of nondominated points is called the Pareto front.

With the criterion for optimality, the crowding distance is chosen to compute the fitness function [12]. The crowding distance can maintain diversity in the population and has good convergence properties.

Following the description of the biologically inspired method, an account of the test cases carred-out in this project is presented next.

2. Test cases

To assess the suitability and efficiency of bioTOM for aerospace design, a number of test cases were selected and simulated. The results obtained in this assessment are summarized in the following sub-sections.

2.1. Cantilever benchmark

The short cantilever problem is a classic benchmark for structural topology optimization [13, 14, 15]. In this problem, a 2×1 cantilever in plane-stress and with a load applied at the free extremity (figure 2) is optimized for minimum weight.

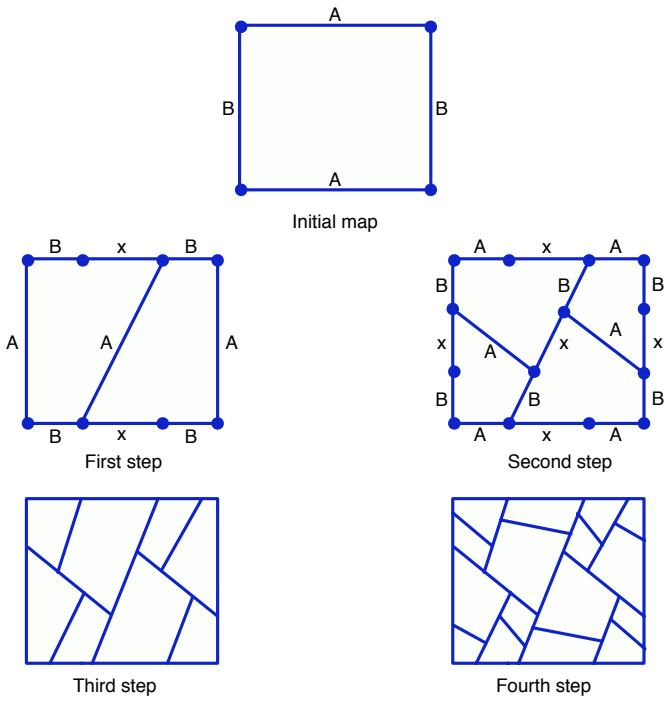

Figure 1: First four steps in the cellular division process modeling the developmental stages of the structure topology.

The Young modulus, E, the point load, P, the density, ρ and the cantilever width w are all set to 1m, while the Poisson ratio, ν, is set to 0.3. These values do not intend to represent any specific material, but rather to provide a simple, yet well defined, benchmark problem to compare the performance of new methodologies against other established approaches.

In words, the objective of this benchmark is to obtain the lightest cantilever's structure for a prescribed maximum deformation. Mathematically the problem can be expressed as:

$$\begin{aligned} &\text{minimize} \quad W(\mathbf{x}) \\ &\text{such that} \quad D_{max}(\mathbf{x}) - D_{lim} \leq 0 \end{aligned} \tag{1}$$

where $W(\mathbf{x})$ is the cantilever's weight nondimensionalized by the weight of the rectangular cantilever 2×1. $D_{max}(\mathbf{x})$ is the maximum displacement and D_{lim} is maximum displacement allowed, in this case D_{lim} is set to 220. Finally $\mathbf{x}$ is the vector that encodes the Map L-system topology as explained previously.

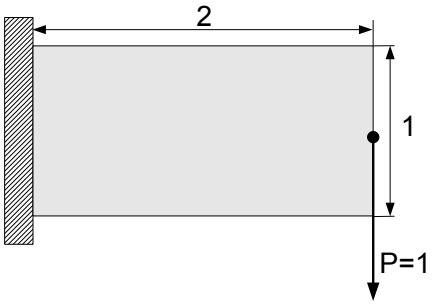

Figure 2: The 2×1 cantilever benchmark.

The fitness value is evaluated with plane stress finite elements available in the FE toolbox COMSOL. This software supports a scripting language similar to MATLAB that is very useful to automatize the calculation of the fitness. Geometry creation, meshing, solving and postprocessing, all can be done through scripting. Some of the commands used are listed bellow.

- `curve2`, creates a 2D curve object in the form of a Bézier curve;
- `elipt2`, creates a solid ellipse/circle;
- `meshinit`, meshes the geometry using the Delaunay triangulation;
- `femstatic`, solves the stationary PDE problem with a nonlinear or linear solver;
- `postint`, integrates expressions over subdomains, boundaries, edges, and vertices;
- `postmin`, computes the minimum value of an expression.

A complete reference for the available commands can be found in the COMSOL user's manual.

This benchmark problem has one constraint and as mentioned previously constraints are enforced through penalization of the fitness values. Thus, the penalization P_w is added to the fitness value in equation 2. P_w is given by:

$$P_w = C\left(e^{\max(D_{max}(\mathbf{x})-D_{lim},0)} - 1\right) \tag{2}$$

with $C = 1$;

The convergence history for the best individual in a generation is shown in figure 3. Initially, the improvement between generations is fast but eventually it flattens out as the best designs become more refined. After 60 generations the

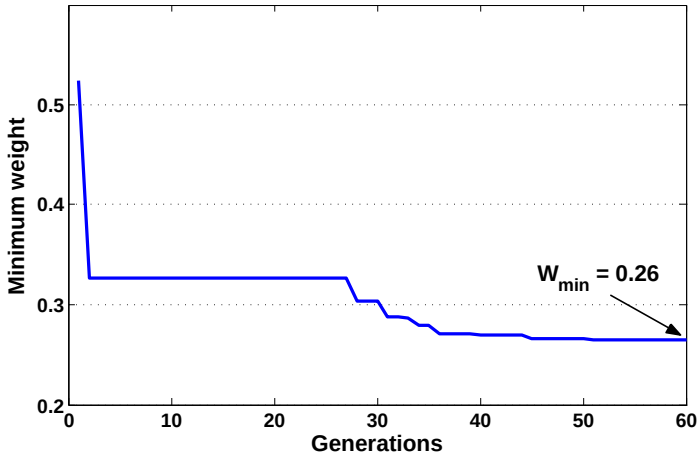

Figure 3: Convergence of the bioTOM for the minimum weight optimization.

lightest cantilever geometry that satisfies the optimization 2 weights $W = 0.26$. This means that with a proper structure, a cantilever with 26% of the mass of the rectangular cantilever from figure 2 exhibits a maximum deformation smaller than D_{lim}. The structure and the Von Mises stresses for this design are shown in figure 4. From these figures it can be seen how the material is placed such that there are no unnecessary elements in structure, i.e., all elements withstand similar level of stress. Also, it can be seen that the elements that are clamped are the thickest ones. This is in agreement with what was expected given that at the cantilever's root the stresses are maximum.

Table 2.1 compares the results obtained with bioTOM against other the results of methods found in the literature: using a bit-array representation [14, 15] or a Voronoi-based representation [13], for the structure. The column W_{min} demonstrates that the optimal structure for the bioTOM represents a significant improvement with respect to the other methodologies. The column $feasible$ shows the percentage of feasible individuals for all generations. As the results of the table shows, bioTOMhas a vital advantage over the Genetic Algorithmof creating feasible desings. This is relevant because the efficiency of the genetic algorithm

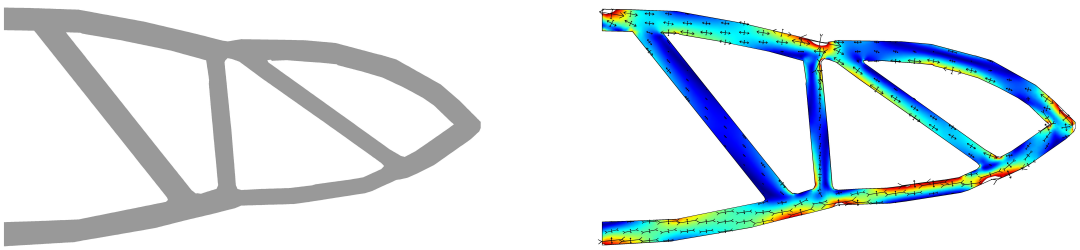

Figure 4: (a) The optimal cantilever's structure for the minimum weight optimization after 60 generations. (b) The colormap shows the Von Mises stresses from 0 to 50 and the arrows represent the principal stresses. Converging pairs represent compressible stresses and diverging pairs represent tension stresses.

improves with increased number of viable individuals. In the Genetic Algorithm, the individuals are not viable, for instance, either because of connectivity problems, or the removal of loaded elements, whereas these defects are prevented in bioTOM. For bit-array representations that ratio can be rather low as shown in the results for [14] whereas for the bioTOM all the individuals are feasible. Another performance measurement is the number of FE evaluations necessary until convergence is achieved. For this problem, the number of FE evaluations necessary for the bioTOM is at lest two orders of magnitudes lower than for the other methods.

	W_{min}	$feasible$	mesh	FE evaluations
bioTOM	0.260	100 %	N/A[1]	~ 300
Wang et al. [14]	0.325	17 %	20×10	~ 20000
Balamurugan et al. [15]	0.340	N/A[2]	20×10	~ 100000
Hamda et al. [13]	0.330	N/A[2]	20×10	~ 16000

[1]Not Applicable
[2]Not Available

Table 1: Comparative analysis of several techniques for the minimum weight problem.

2.2. MAV wing

In this second test case, the problem of dual optimization of mass and performance of a flexible MAV wing is studied. The wing is modeled as a membrane surface (latex rubber) reinforced with a stiffer material (carbon fiber laminates)—the elastic properties for the wing materials are given in table 2.2. The latex membrane determines the wing planform shape and the carbon reinforces the structure. The goal is to simultaneously determine the wing's shapes and structure layouts with best mass and aerodynamic performance; the latter measured by the wing finesse: $L/D = C_L/C_D$, where C_L and C_D are the lift and drag coefficients, respectively.

	Rubber	Carbon
Young Modulus $[GPa]$	$2 \times 10^{-}3$	317.2
Poisson Coefficient	0.5	0.31

Table 2: Properties for the materials used on the wings

To better assess bioTOMagainst existing design methods, the present test case is divided into four parts. In the first three, the shape is fixed and only the topology is optimized. This allowed for a direct comparison between bioTOMand current popular methodologies for topology optimization. Thus a rectangular planform is chosen with a chord equal to $c = 0.15\ cm$ and a span equal to $b = 0.30\ cm$—corresponding to an area of $A = 0.045\ m^2$ and an aspect ratio ($\mathcal{R} = (b)^2/A$) of 2. In the fourth part, the versatility of bioTOM is explored by allowing wing's planform shape to vary, while keeping the wing area constant. For all cases the undeformed shape of the wing is a flat plate and the final wing shape is solely the result of the fluid-structure interaction., m, m^2

The wing is positioned relative to the incoming flow at an angle of attack (α) that is assumed to be fixed and equal to 3° for all cases.

The symmetry of the problem allows to reduce the computational mesh by simulating only one side of the wing. At the symmetry axis, which corresponds to the wing's root, the structure is assumed to be clamped, i.e., zero deformation and zero angular deformation. Figure 5 depicts the problem geometry for the rectangular wing (a) and for the variable shape wing (b). The flow conditions correspond to a Reynolds number of 10^5, a typical value for these kind of aerial vehicles [16]. The Reynolds is defined as $Re = \frac{VL_c\rho}{\mu}$, where L_c is a characteristic length for the problem. For all cases L_c is set to be equal to the chord of the rectangular wing, $L_c = c = 0.15\ m$. The air properties are given below in the

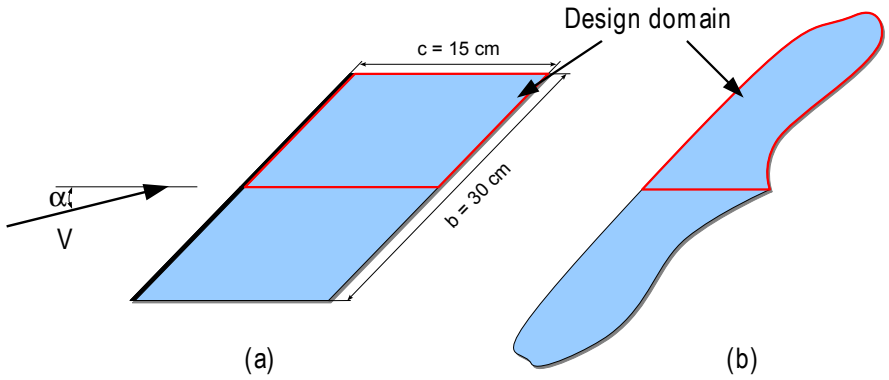

Figure 5: The geometry of the problem: (a) rectangular wing and (b) the wing of variable shape. Both wings have the same planform area. The flow conditions are the same for both cases. The computational domains are highlighted in red.

table 2.2 and correspond to the air properties for the standard atmosphere at sea level. From these values the velocity of the flow can be readily calculated to be $V = 13\ ms^{-1}$.

Viscosity $[kg/sm]$	1.785×10^{-5}
Density $[kgm^{-3}]$	1.225

Table 3: Air properties at sea level for the standard atmosphere.

As previously explained, the topology generated by the Map L-system must be given a physical interpretation. In this test case, the edges represent carbon elements and the interior regions of the cells represent the latex membrane.

The relevant parameters for the Map L-system follow next.

- The initial map is bounded by the rectangle $[0, 0.15] \times [0, 0.15]$ which corresponds to one half of the rectangular wing.
- The number of developmental stages, $NLevels$ is an optimization parameter in the range $[3, 6]$.
- The alphabet Σ contains 8 letters excluding the terminal symbol x.
- The production rules have 8 tokens.

- The special symbol $*$ and / are used to control the edges thickness.
- The equilibrium computation is bypassed.

For the fourth problem, the wing shape is also a design parameter and, as such, it must be encoded in the individual's genome. In this work the shape of the wing is constructed from $2N$ parameters appended to the genome. The first N elements consist on the coordinates (x, y) that define the wing leading edge (L.E.) $\mathbb{P} = \{\mathbf{P}_1, \cdots, \mathbf{P}_N\}$ – see figure 7 where $N = 5$. The other N elements correspond to the wing chords $\mathbb{C} = \{c_1, \cdots, c_N\}$ at the spanwise coordinates given by the x component of $\mathbb{P}$. The trailing edge (T.E.) chordwise coordinates (y direction) are simply given by

$$\mathbb{Q}_y = \{P_{1y} + c_1, \cdots, P_{Ny} + c_N\} \tag{3}$$

and the x coordinates are $\mathbb{Q}_x = \mathbb{P}_x$. The leading edge and trailing edge coordinates are then connected with splines to ensure smooth curves and these two curves are connected at the root and tip by straight lines, forming the closed curve $\mathcal{S}$. This method is unbiased toward any particular kind of wing planform, and can generate a large variability of wing shapes as figure 6 demonstrates.

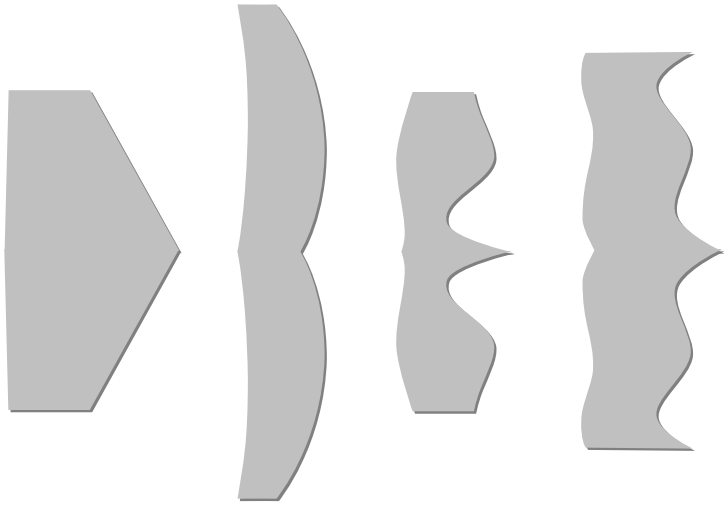

Figure 6: Examples of several wing planforms generated randomly.

With the planform shape $\mathcal{S}$ determined, all the vertices in the Map L-system topology are linearly interpolated such that the square $[0, 0.15] \times [0, 0.15]$ is transformed into the shape $\mathcal{S}$. The outcome is a smooth and complex topology as shown

in figure 7(c). Since after this transformation the wing area and $\mathcal{AR}$ are unspecified values it is necessary to scale the geometry in order to obtain the final topology. The wing $\mathcal{AR}$ is also an optimization parameter encoded in the individuals genotype and it is always within the range $0.5 \leq \mathcal{AR} \leq 10$.

To obtain the desired values for area and $\mathcal{AR}$ the scaling factors in the chordwise direction, X_{sf}, and in the spanwise direction, Y_{sf} are in general distinct, and can be calculated as:

$$\begin{aligned} X_{sf} &= \frac{A}{A_0 Y_{sf}} \\ Y_{sf} &= \frac{b}{b_0} \\ b &= \sqrt{\mathcal{AR}A} \end{aligned} \tag{4}$$

where b_0 and b are the wingspans for before and after the scaling, respectively. A_0 and A are the wing areas for before and after the scaling, respectively. This process is exemplified in figure 7

With the geometry so defined, it is possible now to build the structure model and determine the wing deformation using the FE method for a specific wing load. As mentioned above the edges of the Map L-system topology are interpreted as Euler beams with square cross section made out of carbon laminate. The beams are characterized by the material properties E_c, ν_c, ρ_c and cross section properties: area A_c and moments of area I_y, I_z and J. As opposed to the cantilever problem shown before, here the inner region of the Map L-system has a physical meaning: the different cells represent latex shells characterized by the material properties E_m, ν_m, ρ_m and thickness t_m. The shell thickness is the same for all the four optimizations, $t_m = 0.1\ mm$, but the square cross section of the beams is not fixed. As explained previously, edge properties can also be subjected to the Map L-system production rules. That feature is used in this case to establish the dimensions of the square cross section of each beam. In this case the Map L-system returns for each edge the property *thicknessRatio* which is a value in the range $[1/3, 3]$. That value is used to determined the actual beam thickness given by $t_0 \times$ *thicknessRatio*, where $t_0 = 1\ mm$. Thus the beam thickness varies in the range $[0.33, 3]\ mm$.

The geometry modeling, meshing, solving and postprocessing are done through scripting in COMSOL allowing for the automated study of the wing designs. A study was performed to determine the mesh density necessary to attain mesh

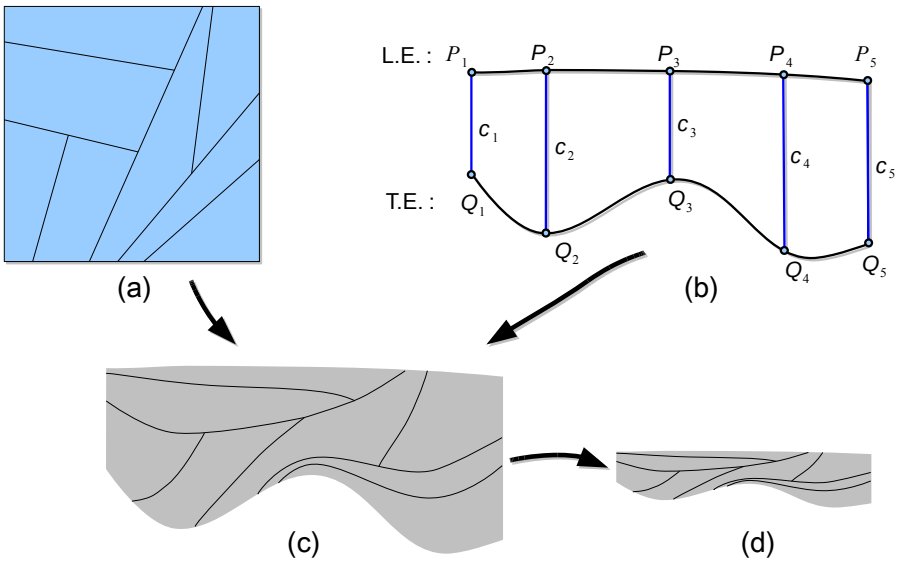

Figure 7: Example that shows how the wing of variable shape is "build" from the Map L-system topology and the shape $\mathcal{S}$.(a) Map L systems topology, (b) wing platform shape $\mathcal{S}$, (c) wing showing the internal structure and (d) the final topology with the correct area and $\mathcal{AR}$, after applying the scaling.

independence—see Figure 8.T ypically, in a 2GHz, 4.00 GB computer the FE method solution is calculated after 2 seconds.

The procedure explained above is independent of the wing load. To obtain the steady state deformation for the wing the aerodynamic pressure loads must be calculated. There are many computational tools that can be used for this calculation, such as, commercial or open source softwares that solve the governing equations – conservation of mass and conservation of momentum, that govern the incompressible viscous flows. These tools can be very accurate but are in general computationally demanding due to the nonlinear nature of the conservation of momentum equations and the necessity of dense meshes in the domain surrounding the wing. Since the bioTOM requires thousands of these computations these tools can not be used due to the prohibiting computational times. As an inexpensive surrogate for the more accurate tools a Vortex Lattice Method (VLM) is used here. The computational effort required by the vortex lattice method is almost negligible when compared to the codes mentioned above given that it requires only the meshing of the wing surface and the solution of a single linear system of

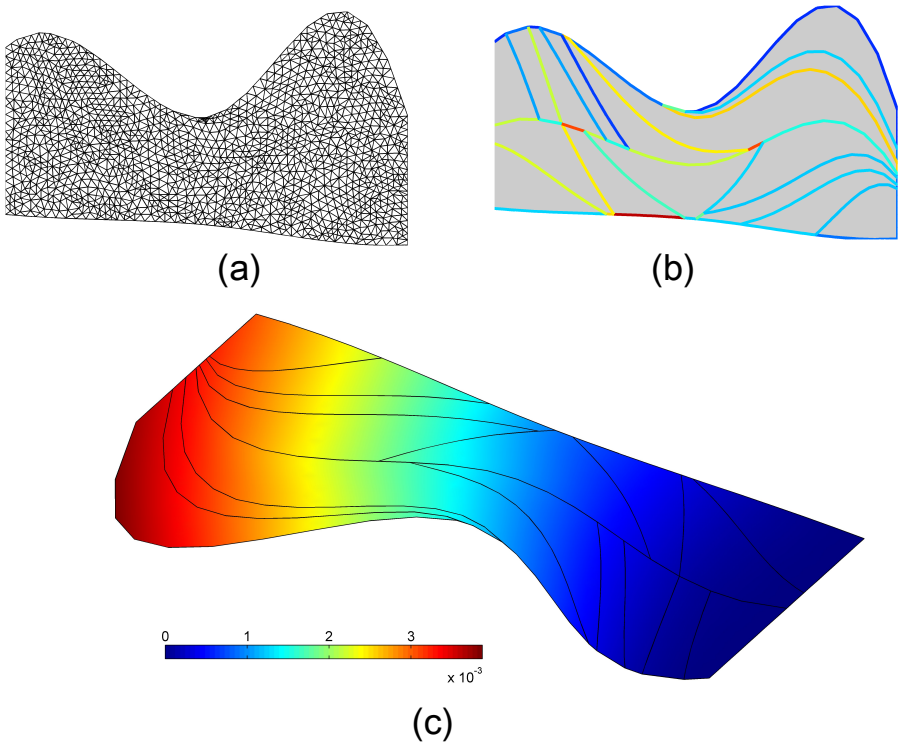

Figure 8: (a) An example of a COMSOL mesh. (b) An example of a COMSOL geometry. The colors represent the edge thickness. Dark red: thick beams, dark blue: thin beams. (c) FE solution. The colormap depicts the wing deformation in m for a constant load of 10 Pa

equations. So that the velocities are given by the gradient of the potential ϕ:

$$\mathbf{v} = \nabla\phi, \tag{5}$$

where the velocity potential is the solution of the Laplace equation

$$\nabla^2\phi = 0, \tag{6}$$

and the boundary conditions are: velocity must tend to the approaching velocity in the farfield

$$\mathbf{v} \rightarrow \{V\cos(\alpha), V\sin(\alpha)\}, \tag{7}$$

and the velocity normal to the wing surface must be zero.

$$\frac{\partial v}{\partial n} = 0. \tag{8}$$

The pressure can be computed from the Bernoulli equation:

$$p_\infty + \frac{\rho V_\infty^2}{2} = p + \frac{\rho V^2}{2}, \tag{9}$$

where $V = |\mathbf{v}|$.

The denomination of vortex lattice method encompasses a myriad of methods. This work uses a linear vortex lattice method as described in [17]. The vortex lattice method approximates the continuous distribution of bound vorticity by discretizing the wing into a paneled grid of N spanwise panels and M chordwise panels as exemplified in figure 9, and placing a vortex ring upon each panel. The vortex ring is created by four vortex filaments located at the edges of the panel. Each vortex filament creates a velocity whose magnitude is assumed to be governed

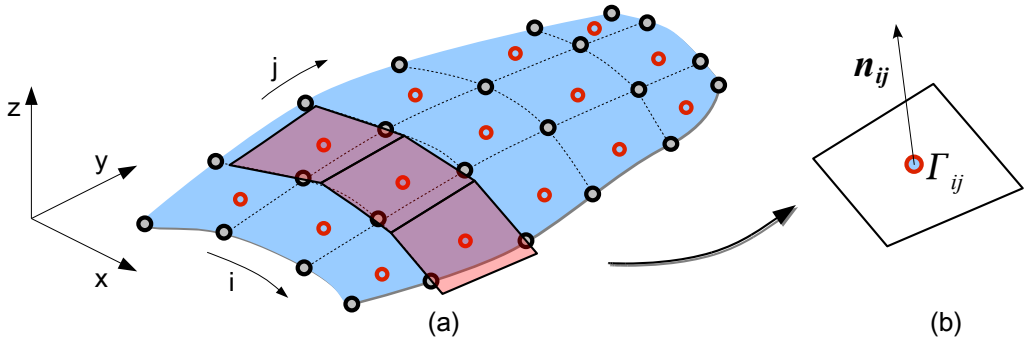

Figure 9: (a) Example of the paneling of a generic wing with $N = 5$ and $M = 3$. The black dots are the wing grid, and the red dots are the points where the vortex is placed – collocation points. Three panels are show. (b) shows a typical panel for which $i = 2$ and $j = 3$. $\mathbf{n}_{ij}$ is the normal vector to the panel ij and Γ_{ij} is the vortex strength $[m^2/s]$.

by the Biot-Savart law [17]. Furthermore, a control point is placed at the three-quarter-chord point of each panel. The tangency condition is applied (i.e., the wing becomes a streamline of the flow) by stipulating that the induced flow (from the vortex rings) along the outward normal at each control point exactly cancels with that caused by the free-stream velocity. The following system of equations results:

$$\begin{pmatrix} a_{11} & a_{12} & \cdots & a_{1m} \\ a_{21} & a_{22} & \cdots & a_{2m} \\ \vdots & \vdots & \ddots & \vdots \\ a_{m1} & a_{m2} & \cdots & a_{mm} \end{pmatrix} \begin{pmatrix} \Gamma_1 \\ \Gamma_2 \\ \vdots \\ \Gamma_m \end{pmatrix} = - \begin{pmatrix} (V\cos(\alpha), 0, V\sin(\alpha)) \cdot \mathbf{n}_1 \\ (V\cos(\alpha), 0, V\sin(\alpha)) \cdot \mathbf{n}_2 \\ \vdots \\ (V\cos(\alpha), 0, V\sin(\alpha)) \cdot \mathbf{n}_m \end{pmatrix} \tag{10}$$

Γ_i is the unknown circulation strength of each vortex ring, and $m = N \times M$. In order to obtain this system of equations the panels must be relabeled in a sequential manner from 0 to $m = N \times M$. For the structured grid that is easily done with the aid of a variable $K = (j-1) \times N + i$. As an example, the panel in figure 9(b) is relabeled from $(2, 3)$ to 12. The elements in the matrix from equation 10 are the influence coefficients, which are given by:

$$a_{ij} = (u_0, v_0, w_0)_{ij} \cdot ni, \tag{11}$$

where $(u_0, v_0, w_0)_{ij}$ are the velocities induced at the *i-th* collocation point by the *j-th*. The indices i and j are sequential indices, each one identifies a different panel. The solution of the linear system (10) yields the strength circulation for each panel. Further details and information can be found in the [17]. Before using the code for the optimization, the code was thoroughly verified against analytical solutions and reference numerical data [17].

At this point the means to calculate the wing deformation for any given out of plane load and the means to determine the aerodynamic load for any given wing geometry are defined. The following step is to incorporate these two solvers in a fluid-structure interaction solver in order to obtain the steady state wing deformation. Given that the FE method here used is the one implemented in the commercial package COMSOL, and the vortex lattice method is coded and compiled in FORTRAN, a segregated solver was used.

The segregated solver was implemented in MATLAB and consists of a fixed point iteration with intermediate update. Thus the aerodynamic load is computed first for the deformed wing and then the wing deformation is calculated for that load and so on. The communication between the FE method and the vortex lattice method is processed through ASCII files.

The loop continues until the stopping criteria are satisfied. In this case the solver stops if the value of the finesse C_L/C_D converges or if the maximum number of iterations is achieved. The last condition is necessary to handle divergence of the segregated approach, which was initially observed for the most compliant structures—the large deformations lead frequently to unstable solutions. For most of these cases a stable solution can be obtained if relaxation is used: the current deformation is a linear interpolation between the deformation from the previous iteration and the one from the current iteration `u = r*uNew + (1-r)*uOld`. Where `r` is the relaxation factor that varies between 0 and 1.

In pseudo code the aeroelastic solver can be written as:

```
ContinueLoop = true
```

```
uNew = 0;
uOld = 0;
u = 0;
it = 1
while ContinueLoop:
    P = computeWingLoad(u)
    uNew = computeWIngDeformation(P)

    if StopLoop == true:
       ContinueLoop = false;
    else:
       ContinueLoop = true;
    endif

    it=it+1;
    u = r*uNew + (1-r)*uOld;
    uOld = uNew;
end while
```

where the relevant subroutines and variables are listed next.

- `u`, `uNew` and `uOld` are the current (relaxed) deformation, the latest deformation and the deformation form the privious iteration, respectively.
- `P` is the current aerodynamic load.
- `ComputeWingLoad`: returns the aerodynamic load for a given wing geometry and deformation.
- `computeWIngDeformation`: returns wing deformation `uNew` for a given wing load `P`.
- `StopLoop`: returns `true` if the one of the stopping criteria is safisfied. Returns `false` otherwise.

Just as in the previous test case, it is necessary to define the objective vector. In this test case, there are two goals: to minimize the wing mass, and to maximize the wing aerodynamic performance as given by the finesse C_L/C_D. The finesse for the deformed wing is calculated as explained previously. The mass of the wing is calculated by integrating the density along the beam cross section or panel

thickness as appropriated. Upon determine these two quantities the fitness of a particular design is determined:

$$\{F(\mathbf{x}), W(\mathbf{x})\} + P_\delta \tag{12}$$

where F is the negative value for the wing's finesse and W is the wing's weight, $\mathbf{x}$ is the vector of reals that encodes the genome and P_δ is the penalization for maximum deformation, given by:

$$P_\delta = 5\left(e^{\max(\delta_{max}-\delta_{lim},0)} - 1\right)$$

The inclusion of this term is necessary given that for individuals with less stiff elements the deformations can be very large, which is not desirable for several reasons. In the first place the validity of the equilibrium equations solved in the FE method might be compromised since they follow from the linear elasticity framework which assumes small deformations. Secondly the wing with large deformations could provoke massive flow separations which would render the vortex lattice method calculations invalid as remarked before. As for stress levels, they are assumed to be small such that there is no risk of material failure and therefore no stress constraint or penalization needs to be considered.

Methodology for the Genetic Algorithm with bit-array representation

For this methodology the wing structure is given by a quadrangular grid of $N \times M$ elements, where N and M are the number of panels in the chordwise and spanwise directions, respectively. This is the same grid used for the vortex lattice method which was previously explained. However, now each grid element also represents a panel or shell as exemplified in figure 11. To each panel is assigned a the value 0 or 1. The former indicates that the material of the panel is latex, and the latter indicates the panel is made of carbon laminate.

The wing deformation is computed with the FE method using shell elements, whose material can be latex or carbon laminate. The material properties are given in table 2.2. An important difference between bioTOM and Genetic Algorithm is that now the carbon laminate is in the form of panels and no longer in the form of beams. The thickness of the carbon laminate panel is the same as the latex panels $t_m = 0.1\ mm$.

The vortex lattice method is exactly as for the bioTOM as well as the aeroelastic solver.

The optimization is performed with the Genetic Algorithm for witch the genome is a vector of $N \times M$ binary elements that determine the wing structure as explained above. Figure 10 exemplifies the decoding for the bit-array representation.

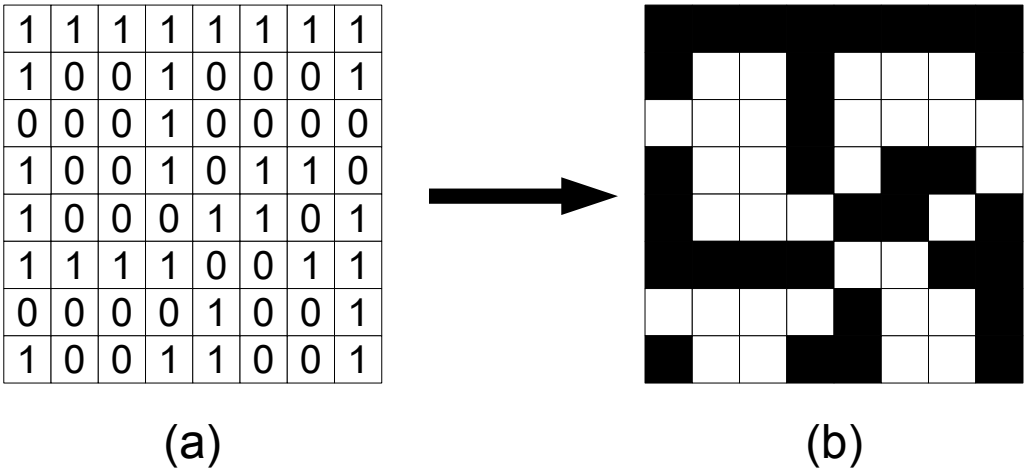

Figure 10: Decoding step for the bit-array representation.(a) The genome; (b) the resulting wing structure: white squares represent latex panel and the black squares represent carbon panels.

Methodology for the gradient method with SIMP

Here the solid isotropic material with penalization (SIMP) method is briefly outline. The interested reader may consult [18], [16]. For this method, the topology of the wing is defined in a similar way to the bit-array representation. The main difference is that to each panel is assigned a value that varies between 0 and 1. This value, for a given panel i, $1 \leq i \leq M \times N$, represents the density variable X_i, where the word density stands for the relative percentage of each material. For example, a density value of $X_i = 0$ means that the panel i is made out of latex membrane, a density value of $X_i = 1$ represents a panel made out of carbon laminate and an intermediate value represents a theoretical inexistent material that is a mix of both. The efficiency of this method increases when $\mathbf{X}$ is penalized [18]. Penalization is accomplished by replacing the changing the density from X_i to X_i^p, where $p > 0$ is the penalization power.

The usage of an inexistent material arises from the necessity of having a smooth function that can be optimized using the gradient method. This is a theoretical artifice that has been widely and successfully used in topology optimization [18].

Formally the problem can be stated as:

$$\begin{aligned} \text{minimize} \quad & F(\mathbf{x}), \mathbf{x} \\ \text{such that} \quad & W(\mathbf{x}) = -W_{lim} \end{aligned} \tag{13}$$

where F and W are the negative of the finesse and the wing's weight as defined

previously. In this case the exact expressions for the mass constraint can be easily obtained:

$$m = \sum_{i=1}^{N \times M} m_i \tag{14}$$

where m_i is the mass of the *i-th* panel which is given by

$$m_i = X_i \cdot m_c + (1 - X_i) \cdot m_m \tag{15}$$

where m_c and m_m correspond to the mass of the carbon laminate panel and to the mass of the latex panel, respectively. Replacing 15 in to 14 yields a linear equation for the constraint.

$$m = \sum_{i=1}^{N \times M} X_i \cdot m_{c_i} + (1 - X_i) m_{m_i} \tag{16}$$

which can be recast as:

$$\begin{pmatrix} 1 & 1 & \cdots & 1 & 1 \end{pmatrix} \begin{pmatrix} X_1 \\ X_2 \\ \vdots \\ X_{N \times M} \end{pmatrix} = \frac{m - N \times M \cdot m_m}{m_c - m_m} \tag{17}$$

The optimization was done keeping the mass constant and maximizing the finesse.

$$\frac{\partial F}{\partial \mathbf{X}} \tag{18}$$

For a given $\mathbf{X}$ the finesses is calculated with the areoelastic solver explained previously. The only difference is that now, for the FE method calculation the material properties for the shell elements are those of the fictitious material determined by the X_i. In practical terms the stiffness matrix $\mathbf{K}_e$ of each finite element is given by:

$$\mathbf{K}_e = (\mathbf{K}_c - \mathbf{K}_m) \cdot X_e^p + \mathbf{K}_m \tag{19}$$

where X_e is the density of the element, and p is the nonlinear penalization power.

With the structure determined as exemplified in figure 11, the wing deformation is computed using the FE method implemented in MATLAB[1]. The grid for the FE method consists in a triangular mesh that is obtained by bisecting each panel diagonally as depicted in figure 11(c). For the results displayed next $N = M = 30$,

[1]The PIs thank Bret Stanford for providing the initial SIMP code.

which yields 900 panels. These figures were dictated mainly because of computational limitations, ideally more elements would be desired for reasons of grid resolution, since the distribution of membrane and carbon elements is dependent on the size of the panels.

Here it should be pointed out a major difference between the bioTOM and the other two methodologies: the mesh independence that characterizes the bioTOM. Indeed, nowhere in the bioTOM formulation a mesh or ground structure is necessary. That has a tremendous effect on the maximum resolution—in the sense of the smallest element on the wing structure—that the structure can display. For the non-bioTOM approaches such as these two the resolution is determined by the grid, in this case with the mesh of 30 elements per side, the resolution is $150/30 = 5\ mm$, whereas for the bioTOM that value is only dependent on the limits imposed by the user. As explained above the bioTOM smallest element can be $0.33\ mm$. To obtain that resolution with a mesh such as the ones here used, 455 elements per side would be necessary, yielding a total of $207,025$ panels. A grid this fine would be computational prohibitive.

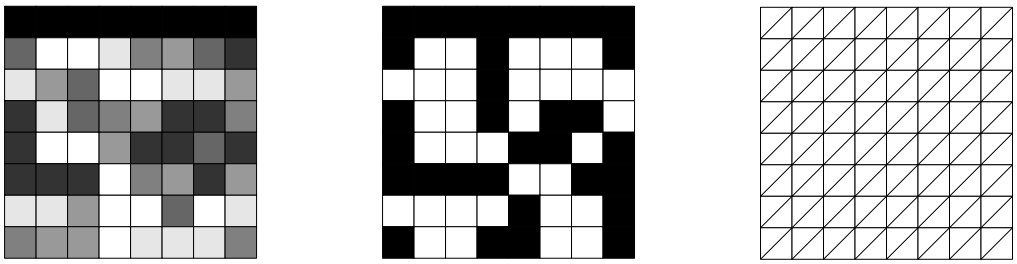

Figure 11: Wing structure for the **Optimization 1** (a) and **Optimization 2** (b). The grey colormap represent the density variable X. Black is for 1 and white is 0. (c) depicts the triangular mesh for the FE method. In this example $N = M = 8$.

In the following, the results for the four optimizations are presented. First it is shown the results obtained with the SIMP then the results for the Genetic Algorithm with a bit-array representation and finally, it is presented the result for the bioTOM. For reference, at this flight condition the finesse for a rigid rectangular wing is equal to 2.49.

The optimization with SIMP ran for 100 iterations or until the finesse converges. A typical convergence history is shown in figure 12.

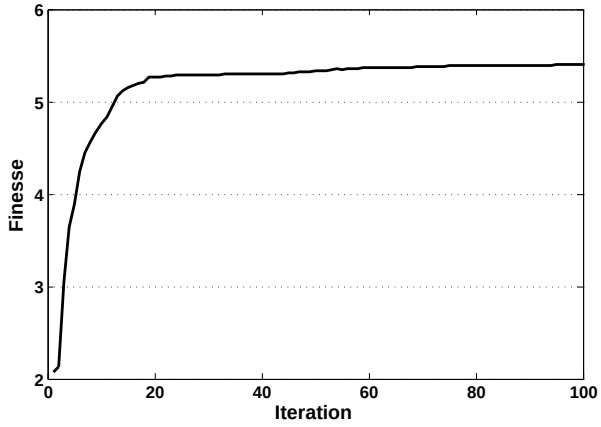

Figure 12: Convergence history for the finesse optimization.

Several values for the mass were studied spanning from a wing made out of latex to a wing made out of carbon. For easy of reading, in the results below the mass is represented by the percentage carbon laminate coverage.

As explained previously, the output of the minimization is the vector of densities $\mathbf{X}$ which requires post processing given that values between 0 and 1 represent a fictitious material. This is a well know limitation of homogeneous methods and there are several techniques to addresses this issue [16]. Here a post-processing is employed by applying the transformation to the elements X_i:

$$X_i = \begin{cases} 0 & \text{if } X_i \leq \epsilon \\ 1 & \text{if } X_i > \epsilon \end{cases} \tag{20}$$

where ϵ is a parameter controlled by the user. In the results that follow $\epsilon = 0.5$ which corresponds to rounding the elements of $\mathbf{X}$. This correction alters the structure and the finesse as shown in figure 13, but maintain the correct trend. In this figure the gray line refers to the results without postprocessing and is shown just for reference since it represents fictitious structures. The "true" results are shown in black. Figure 14 shows the best wing structure of all cases studied. The optimum level of carbon laminate coverage was found to be approximate 30% without postprocessing – figure 14(a). After the postprocessing – figure 14(a), the percentage of carbon laminate decreases to 20% but the finesse remains almost the same at 5.4 as shown in figure fg:bestSimp.

This figure clearly shows that there is a optimum level of carbon coverage such that the wing is neither to stiff nor to compliant.

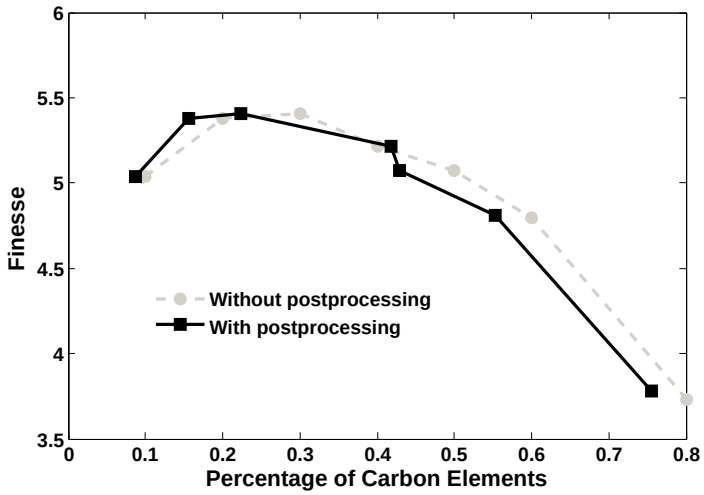

Figure 13: The finesse variation with the carbon laminate coverage.

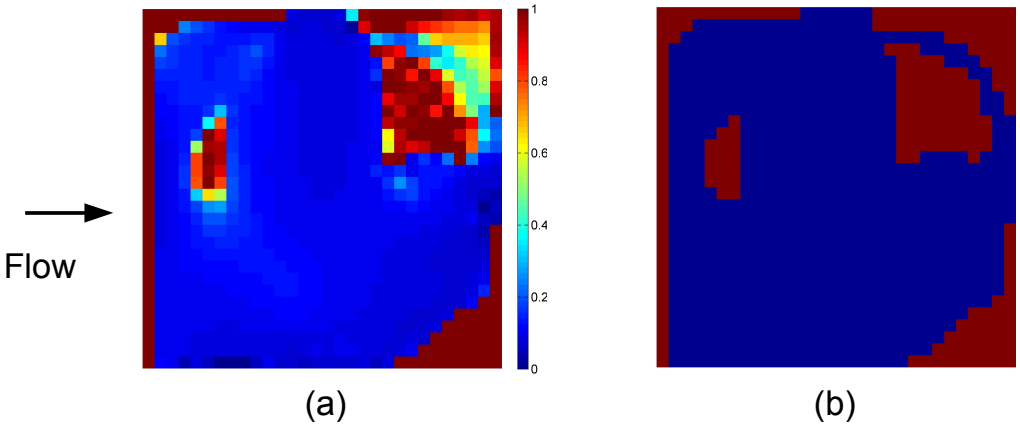

Figure 14: Best wing structure. Only half of the wing is shown. The arrow shows the flow direction.(a) Without postprocessing, (b) with postprocessing

In this segment, the results for the square wing optimized with the Genetic Algorithm and the bit-array representation for the wing's structure are presented. The Genetic Algorithm ran for 100 generations of 200 individuals. Figure 16 shows all the individuals calculated during the simulations. The Pareto front is highlighted in blue. The horizontal axis represents the designs finesse and the vertical axis represents the wing's mass. Given that the carbon coverage is a

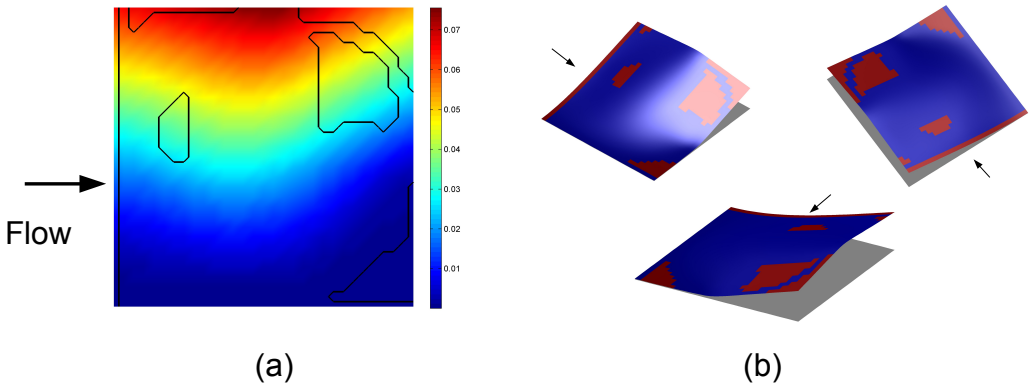

Figure 15: The wing deformation for the best structure. (a) The color map shows the wing deformation in m. The contours identify carbon laminate regions.(b) Three different perspective views of the wing deformation. The arrows show the incoming flow direction for orientation.

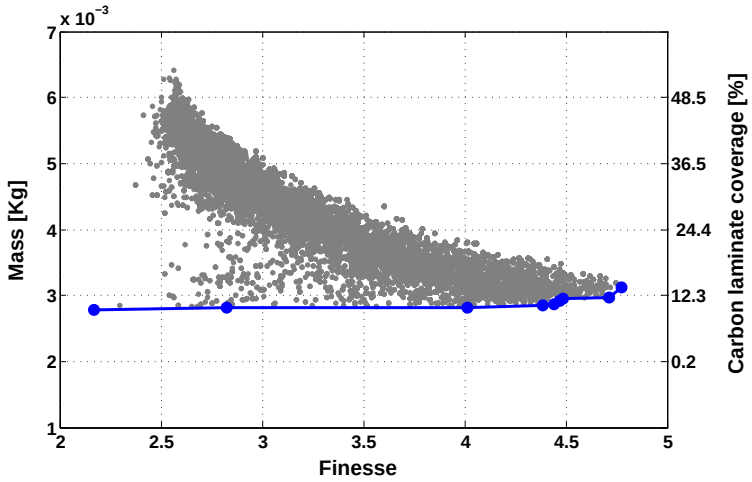

Figure 16: Pareto front for Genetic Algorithm with the bit-array representation.

relevant parameter as demonstrated previously, that value can be read in the left vertical axis.

There are nine designs in the Pareto front. Depending on design goals any of these individuals can be selected. Three of these designs order form highest to lowest finesse can be seen in figures 17, 18 and 19.

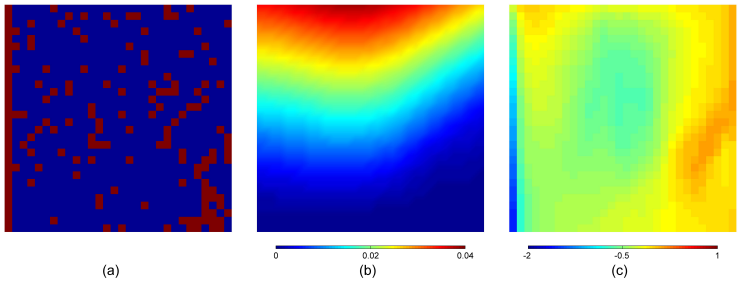

Figure 17: Pareto front.

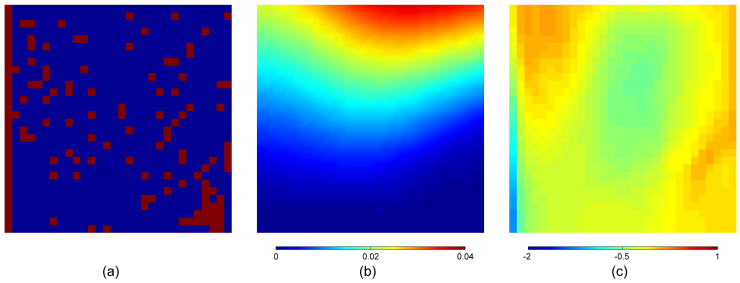

Figure 18: Pareto front.

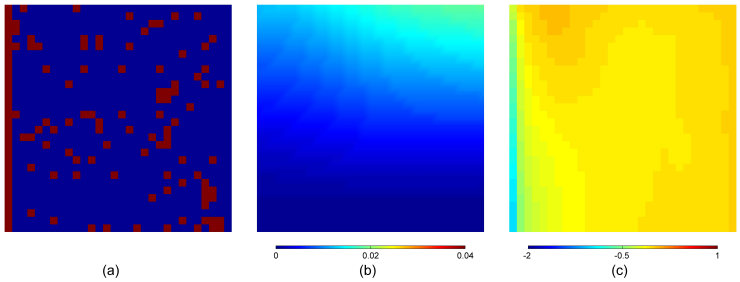

Figure 19: Pareto front.

The results for the multiobjective bioTOM optimization for the square wing follow next. These results were obtained with 100 generations of 200 individuals. All individual whose fitness are in the range $[1, 6] \times [0.001, 0.007]$ are shown in figure 20. The Pareto front is displayed in blue. The imediate conclusion by comparing to the results from the two previous results is that the bioTOM finds designs whose finesse is as good as the ones for the SIMP, but as the mass decreases bioTOM

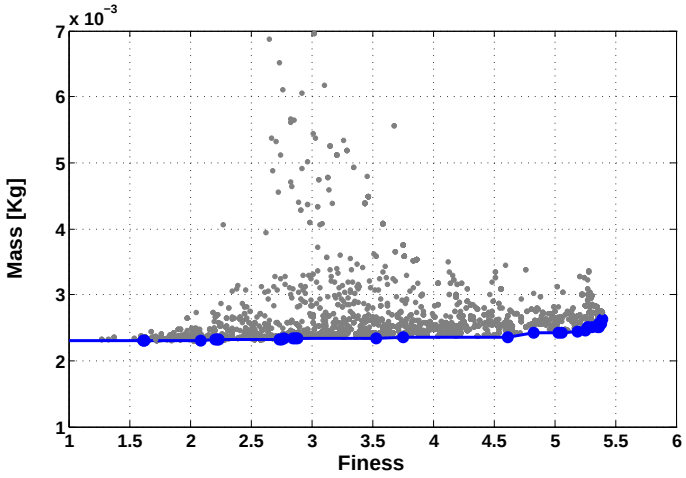

Figure 20: Pareto front for Genetic Algorithm with the bit-array representation.

outperforms SIMP. Three different designs are shown in figures 21 to 23. Each panel shows from left to right: the wing design with the carbon beams colored by their thickness in mm, the steady-state wing deformation in m and the pressure coefficient. This designs are striking for their simplicity. Indeed the evolutionary

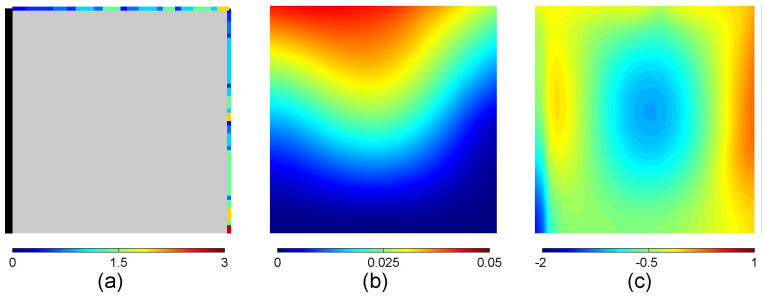

Figure 21: Pareto front design: finess=5.40, mass=0.0026.

algorithm shows that very few to none beams are necessary within the wing. All emphasis is in the beams at the edge of the wing. Figure 24 displays the structure of the wing with carbon beams of different thicknesses for the design with the best finesse.

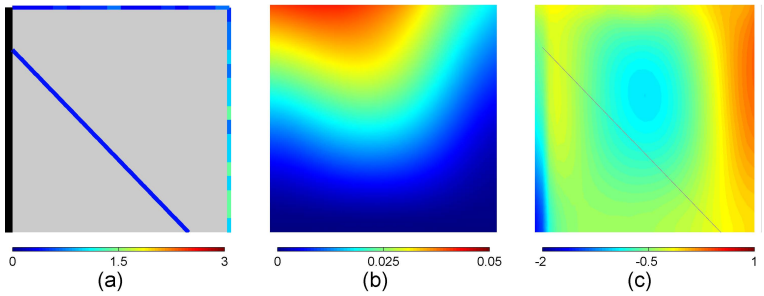

Figure 22: Pareto front design: finess=5.26, mass=0.0025

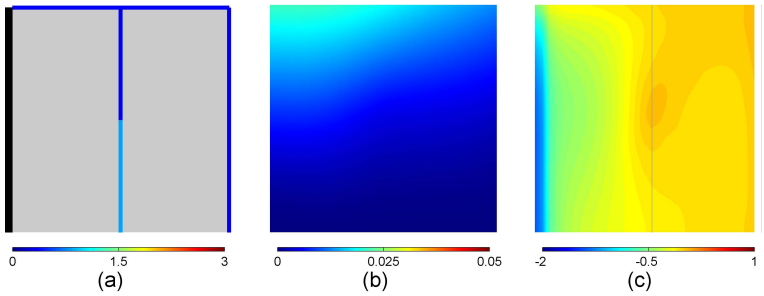

Figure 23: Pareto front design: finess=3, 53, mass=0.0023

Finally the results for the wing with a variable shape are shown. The optimization was ran with a population of two hundred individuals and for one hundred generations. Figure 25 shows all designs studied whose fitness vector falls in the range $[0, 10] \times [0, 0.01]$. Some Pareto designs are shown in figures 26-29. Each of these figures depicts: the (a) the wing geometry or skeleton with the beams thickness given by the colormap; (b) the wing deformation in *meters*; and (c) the pressure coefficient distribution. All the figures assume the same color maps. These figures are shown in descending order of finesse.

The amplification factor is not the same for every figure, or otherwise some figures would be very small because the wing $\mathcal{AR}$ differs from design to design, hence the wing shapes can not be compared using these figures. Figure 30 depicts the wing designs in the same scale. The labels in this figure show the wing aspect

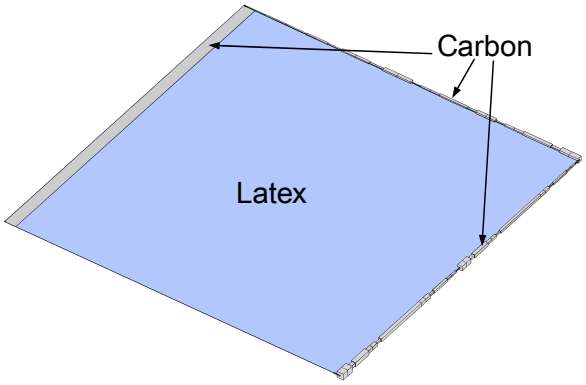

Figure 24: The actual wing structure showing the carbon beams with different thicknesses.

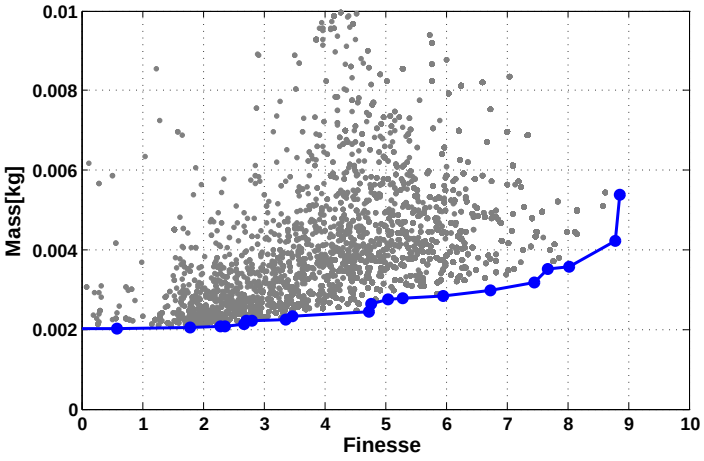

Figure 25: Pareto front and accumulated population at the one hundredth generation.

ratio, $\mathcal{AR}$.

The layouts on the Pareto front conveys a trend for increased "area coverage" by the reinforcements as more mass becomes available. Thus, small mass Pareto designs tend to concentrate their limited mass along critical axes, whereas with more mass available the the number and spread of reinforcements increase. This increase in area coverage with more mass available can be understood by noticing that, at low mass, spreading this low amount of reinforcement throughout the wing

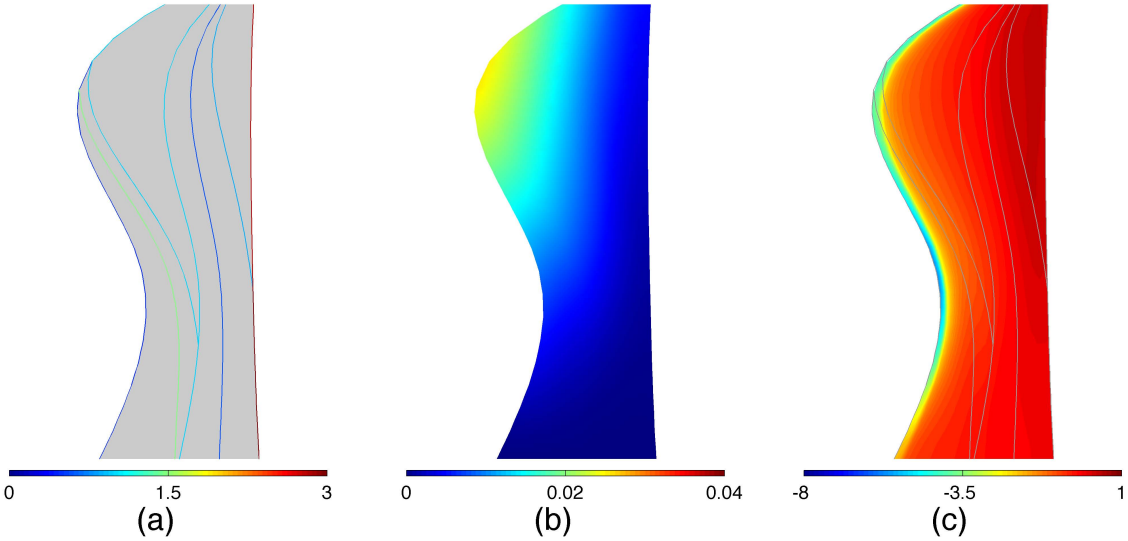

Figure 26: Pareto design: finess=8.87, mass=0.0054. (a) geometry. The color bar represents the beams thickness in mm. (b) wing displacement in m. (c) pressure coefficient.

box area would not strengthen any specific wing region. And would, as a consequence, provide little stress relief on the wing box. By contrast, with increased mass available, the topology can strengthen the critical axes of the structure and also reduce the stress with reinforcements that work together to distribute the load amon

3. Fighter wing box

This next test case consider the problem of the design of the wing box of a generic aircraft fighter. As before, the topology generated by the map L systems is a planar topology with no canonical structural meaning attached to it—in the sequel, this topology is called the structure skeleton. To build a structure model from this topology, first it is selected the following basic structural elements:

- Shear panels;
- Posts and caps for each shear panel.
- Upper and lower skin shells connected to the shear panels.

The shear panels are structural elements that can support shear stress and extensional force along its edges. These elements have negligible bending stiffness

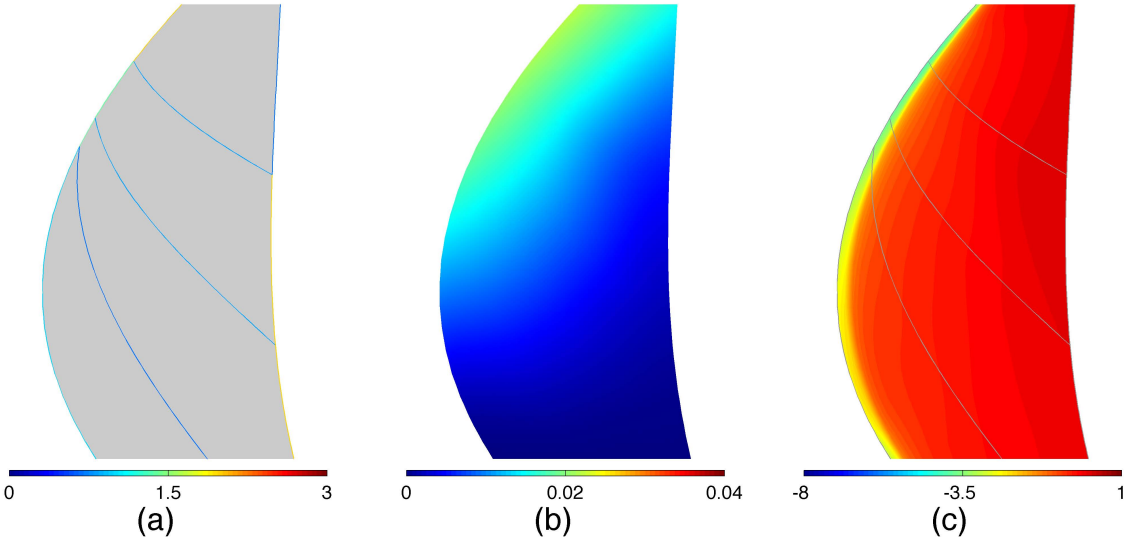

Figure 27: Pareto design: finess=7.67, mass=0.0035. (a) geometry. The color bar represents the beam's thickness in mm. (b) wing displacement in m. (c) pressure coefficient on the wing.

and axial membrane stiffness. The posts and caps are rod elements that connect the shear panels and shells, and they have negligible bending stiffness. The upper and lower skins are modeled as isotropic shells.

These basic structural elements are then combined into a structural model for the wing box. The resulting wing box is simulated using the finite-element method [19, 20, 21]. The final finite element model is explained and illustrated below for the wing box structure of a generic aircraft fighter. In the present test case, because of its widespread use in the aeronautical industry, the FE model was created and simulated using MSC/NASTRAN™. This choice also highlights the versatility of bioTOM in working with existing software, with minimum modification.

The specific steps leading to the finite element model of the wing box are enumerated below.

1. **Mesh generation.** Given a layout, in this first step, a two-dimensional mesh is generated that conforms with the planar topology—see figure 31. For that purpose, an advancing front, Delaunay triangulation method [19] is used. The result is a set of two-dimensional grid points, and the adjacency matrices for the nodes, edges and faces of the discretized domain. In the

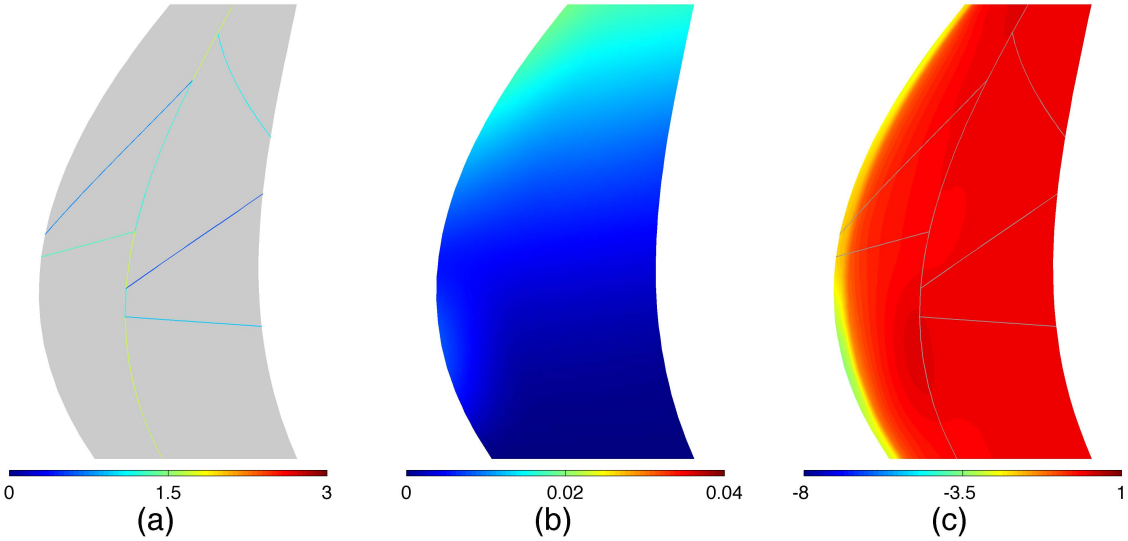

Figure 28: Pareto design: finess=5.29, mass=0.0028. (a) geometry. The color bar represents the beam's thickness in mm. (b) wing displacement in m. (c) pressure coefficient on the wing.

NASTRAN™ card deck, the "GRID" points are written in the three dimensional space by symmetrically placing the grid points above and below the wing symmetry plane—the z-coordinate of each point is obtained according to an interpolation function that accounts for the variation of the wing thickness.

2. **Shear panels.** After the grid points have been created, as a second step, the cards for the shear panels as "CSHEAR" elements are written. These elements are specified as quadrilaterals using the grid points generated in the first step. The thickness of each shear panel is a function of the edge in the skeleton onto which the panel projects. In figure 32 it is shown the shear panels for the mesh generated in the first step.

3. **Posts and caps.** In this third step, the shear panels defined previously are strengthened with posts and caps. The latter are rods that are modeled as "CROD" finite elements in NASTRAN™. Each post is placed at the vertices of the skeleton and the caps run at the lower and upper edges of the shear panels. The radius of each cap is the same for each edge of the skeleton. The elements thus generated are illustrated in figure 33.

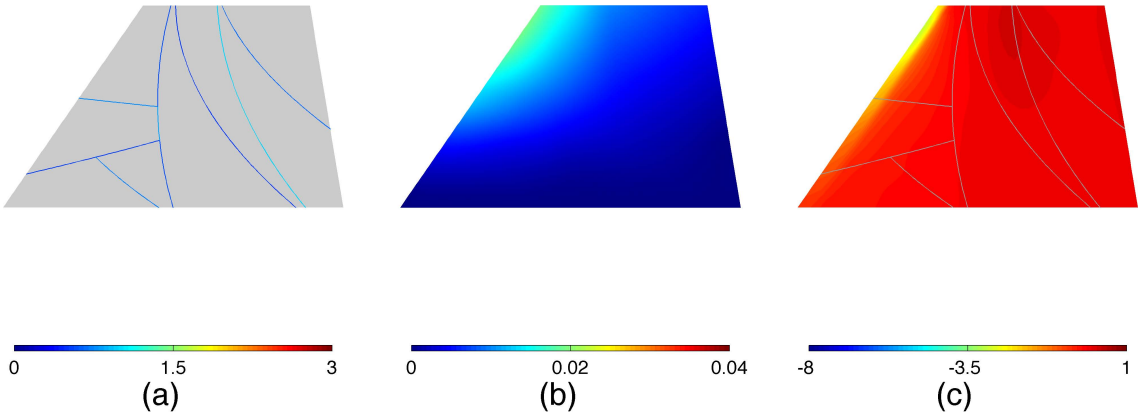

Figure 29: Pareto design: finess=3.48, mass=0.0021. (a) geometry. The color bar represents the beam's thickness in mm. (b) wing displacement in m. (c) pressure coefficient on the wing.

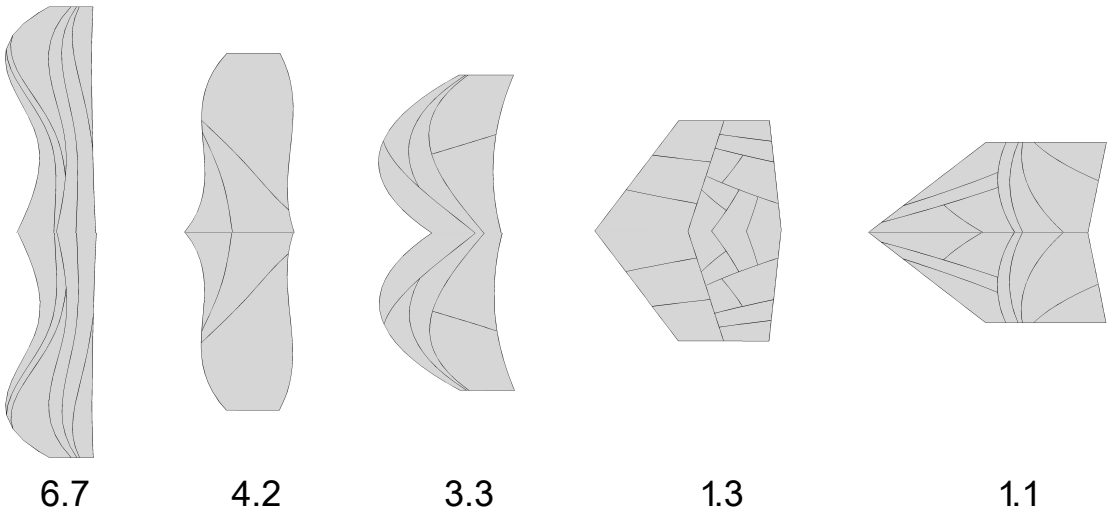

Figure 30: Individuals from the Pareto front. The label is the $\mathcal{AR}$ of the wing.

4. **Upper and lower skins.** Finally, the wing box is closed with upper

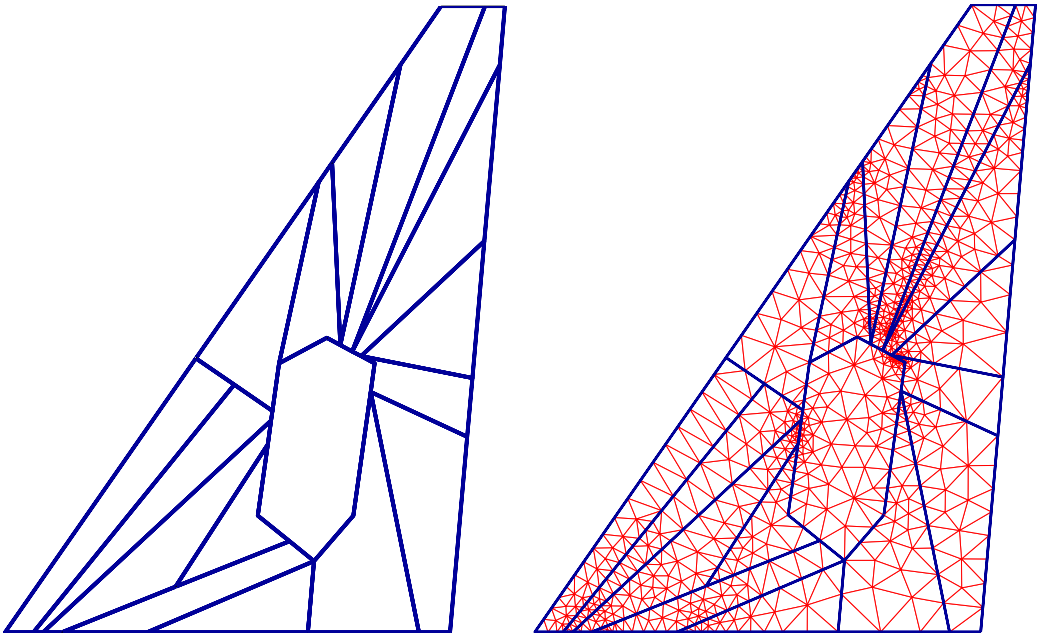

Figure 31: Skeleton (left) of wing box design and the generated mesh (right).

and lower skins. Both skins are modeled by triangular shell elements of "CTRIA3" type in NASTRAN™ with equal in- and out-plane stiffness. The complete structural model is depicted in figure 34.

With the structural model, the analysis can be performed using NASTRAN™ to obtain the desired information on deformation, stress and mass of the structure. Figure 35 shows the simulation result for the static aeroelastic problem of the trim problem in a six-gravity maneuver—see §**??** for details on the physical problem.

The geometry of the problem consist of a sweep and tapered wing with an internal polygonal area whose boundary the structural elements cannot cross—see figure 36. In this problem, the polygon area inside the planform represents the area that delimits a generic aircraft subsystem. All components of the wing are build with the same material with assumed properties: $E = 1 \times 10^7$ psi and $\nu = 0.33$. The flight condition corresponds to the trim condition for a vertical, six-gravity maneuver at sea-level and Mach number $M = 0.7$. The dynamic pressure

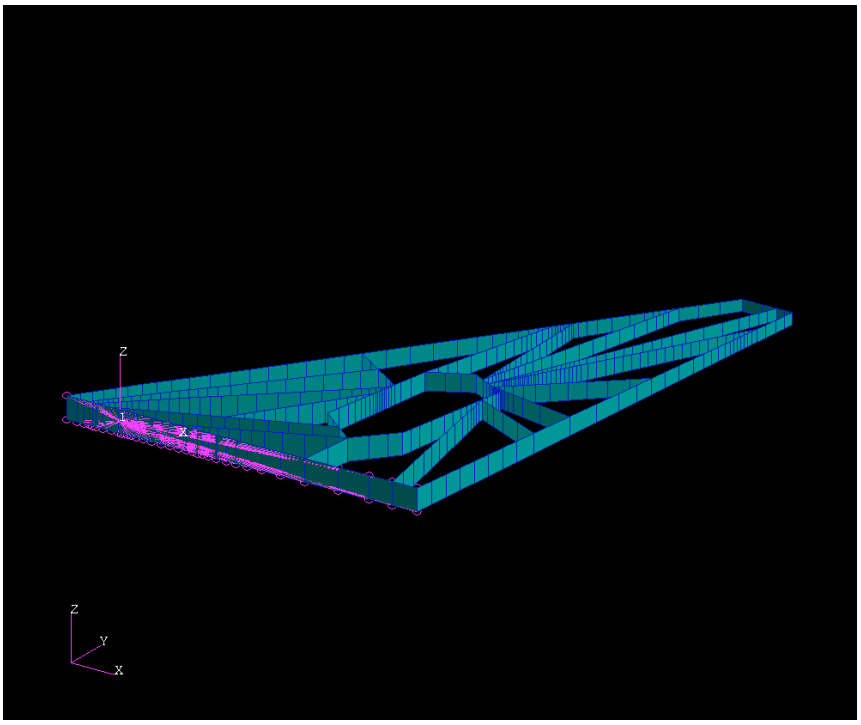

Figure 32: Shear panel elements in the wing box model.

is $q = 20\,\mathsf{psi}$. The aerodynamic load is calculated using the Doublet-Latice Method for interfering lifting surfaces in subsonic flow [22, 23]. Besides the aerodynamic loads, a concentrated mass of $2000\,\mathsf{lbm}$ at $x = 94.15\,\mathsf{in}$, $y = 47.05\,\mathsf{in}$, $z = -2.56\,\mathsf{in}$, a concentrated mass at the support point at the root: $x = 40\,\mathsf{in}$, $y = 0\,\mathsf{in}$, $z = 0\,\mathsf{in}$ and a concentrated load of $1000\,\mathsf{lbf}$ at the positive Oz-direction at the tip point $x = 135.31\,\mathsf{in}$, $y = 138.20\,\mathsf{in}$, $z = 1.51\,\mathsf{in}$ are considered. The distributed body gravitational force field is also accounted for and an inertial, non-structural added mass distributed over the wing is used to account for inertia effects: the "inertia

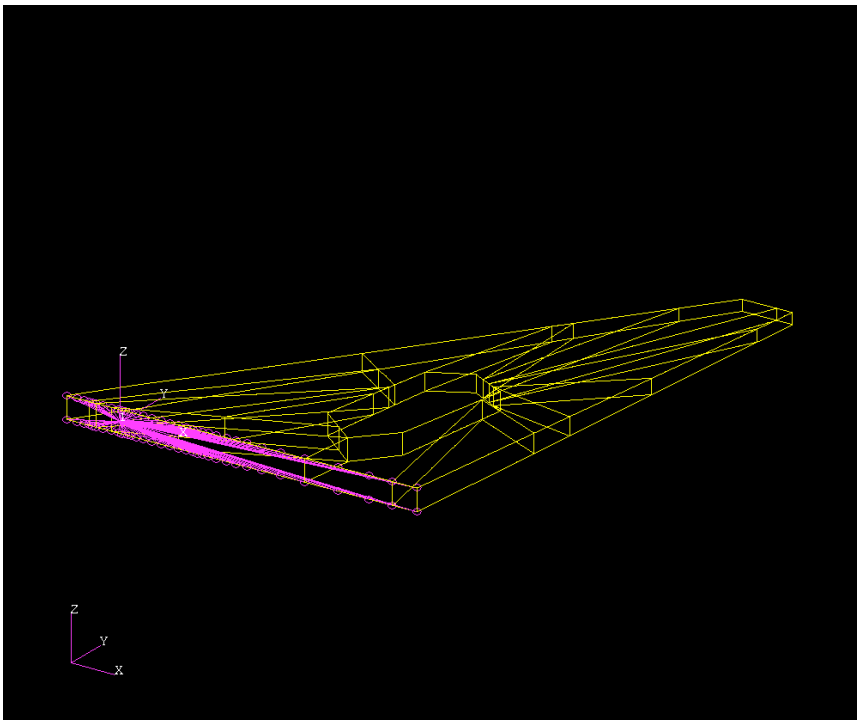

Figure 33: Post and cap elements in the wing box model.

relief" from NATSRAN™.

The optimization was run with a population of two hundred individuals and for fifty generations. In the runs, rules defined by six token slots, and symbols controlling each of the following structure properties: post radius, cap radius, skin thickness and shear panel thickness are used. The vector of design variables comprised the mass of the structure and the maximum stress on the structure. The latter is calculated among the maximum von Mises stress in the skins, the maximum axial stress on the rods and the maximum shear stress in the shear

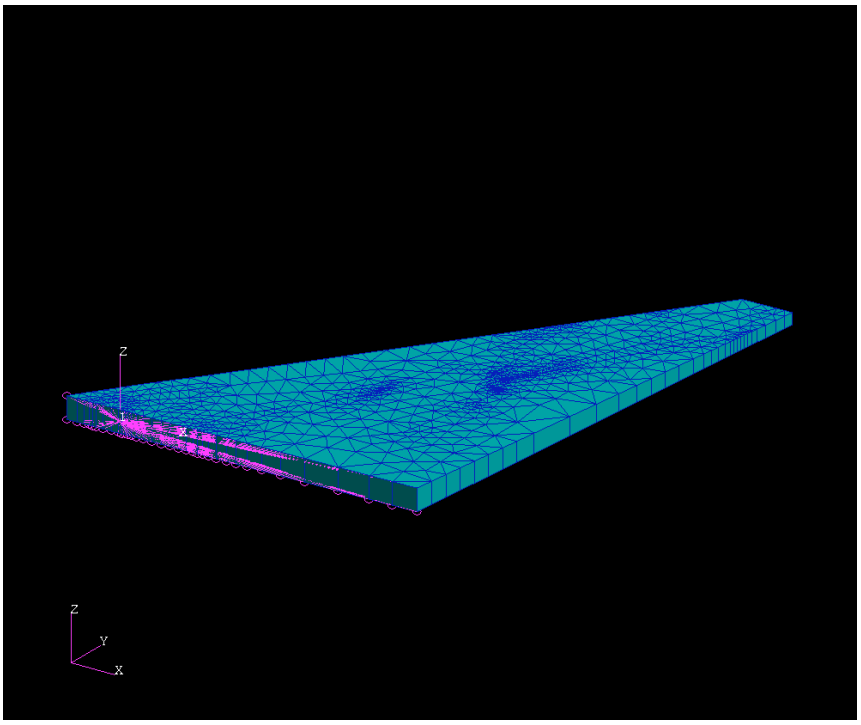

Figure 34: Upper and lower skins and the final wing box model.

panels.

Figure 37 shows the Pareto front and all individuals calculated in the fifty generations, whose normalized fitness vector fall in the unit $[0, 1]^2$ square. The normalization is effected using a reference mass of $1500\,\mathsf{lbm}$ and the allowable shear stress for aluminum $12,000\,\mathsf{lbm}$.

A sample of Pareto designs is shown in figures 38–45. Each of these figures depicts the skeleton on the left and the von Mises stresses on the deformed structure at the right. The displacement is amplified for easy of reading—note that each

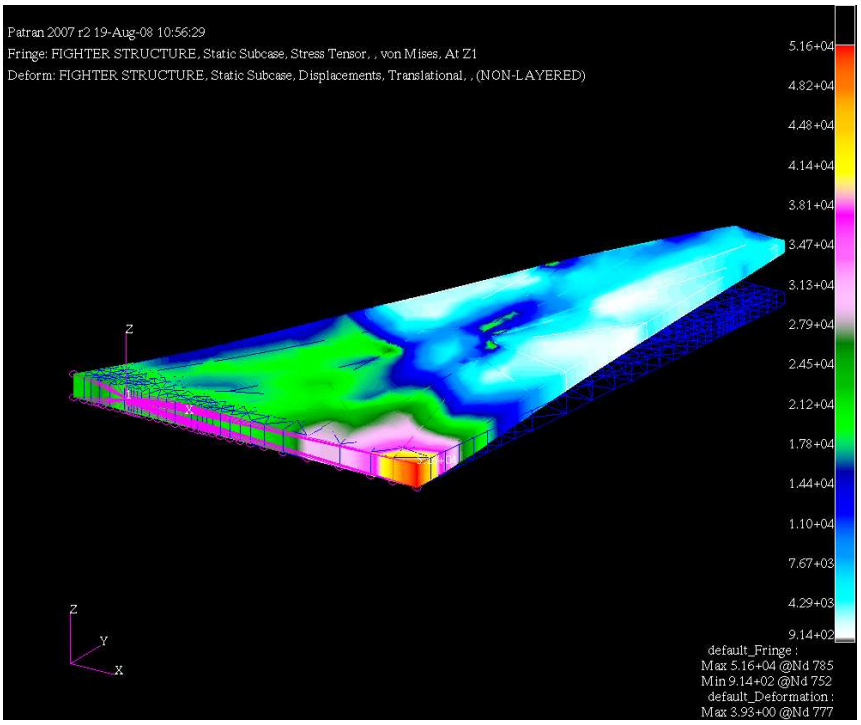

Figure 35: Von Mises stress distribution for the wing box model.

figure assumes a different color map and different amplification ratio. These figures are shown in descending order of mass, and both the normalized mass and the normalized stress are shown in the caption as a percentage of their respective normalizing factors.

The layouts on the Pareto front conveys again a trend for increased "area coverage" by the reinforcements as more mass becomes available. Thus, small mass Pareto designs tend to concentrate their limited mass along critical axes, whereas with more mass available the number and spread of reinforcements increase. This

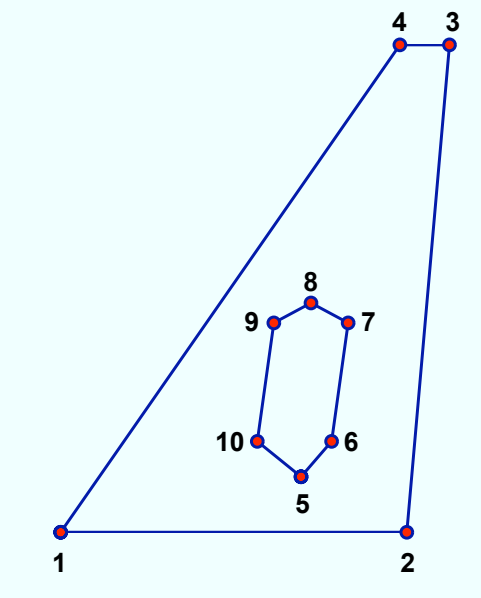

Figure 36: Schematic of the wing-box horizontal projection. Coordinates (x, y) of the geometry vertices: **1**: $(25.0000, 0.00000)$, **2**: $(123.222, 0.00000)$, **3**: $(135.313, 138.200)$, **4**: $(121.260, 138.200)$, **5**: $(93.2080, 15.7500)$, **6**: $(101.877, 25.7500)$, **7**: $(106.570, 59.3750)$, **8**: $(96.0300, 65.0000)$, **9**: $(85.4890, 59.3750)$, **10**: $(80.7960, 25.7500)$. Length in inches.

increase in area coverage with more mass available can again be understood by noticing that, at low mass, spreading this low amount of reinforcement throughout the wing box area would not strengthen any specific wing region. And would, as a consequence, provide little stress relief on the wing box. By contrast, with increased mass available, the topology can strengthen the critical axes of the structure and also reduce the stress with reinforcements that work together to distribute

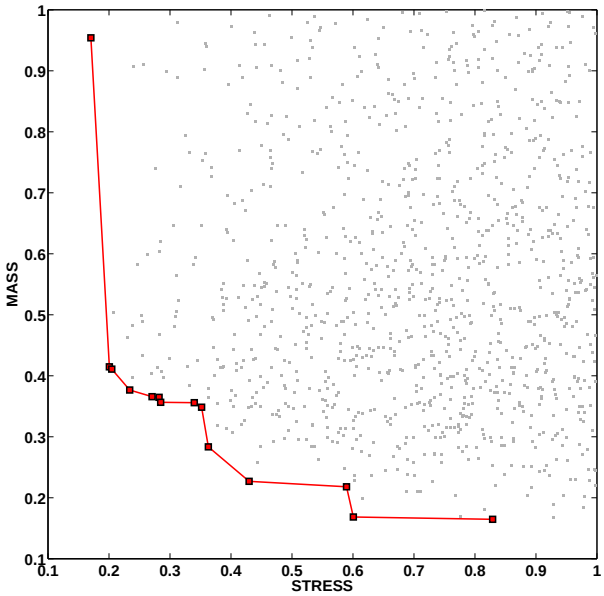

Figure 37: Pareto front and accumulated population at the fiftieth generation.

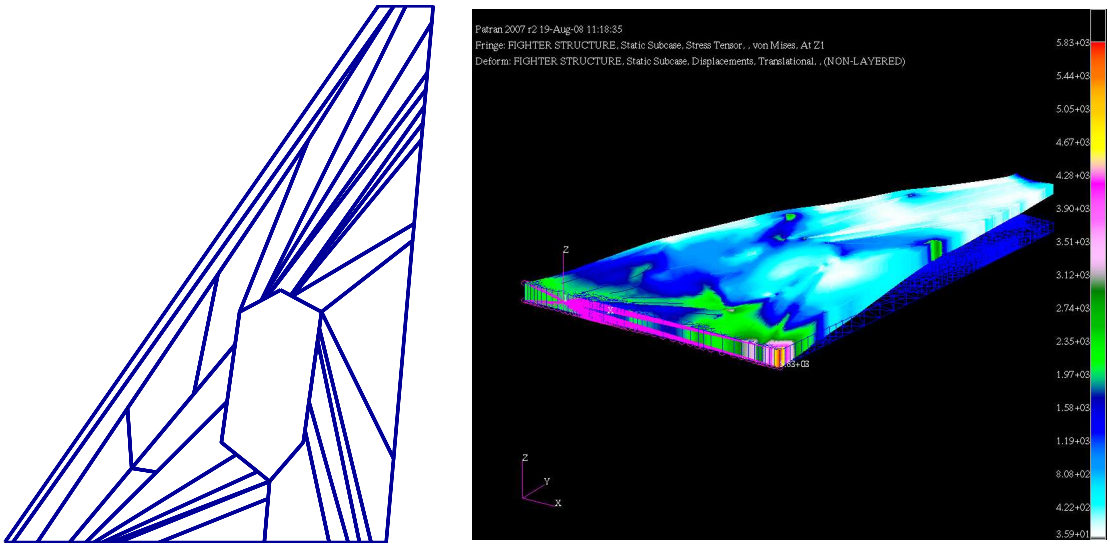

Figure 38: Pareto design: mass = 95.4 %, stress = 17.2 %.

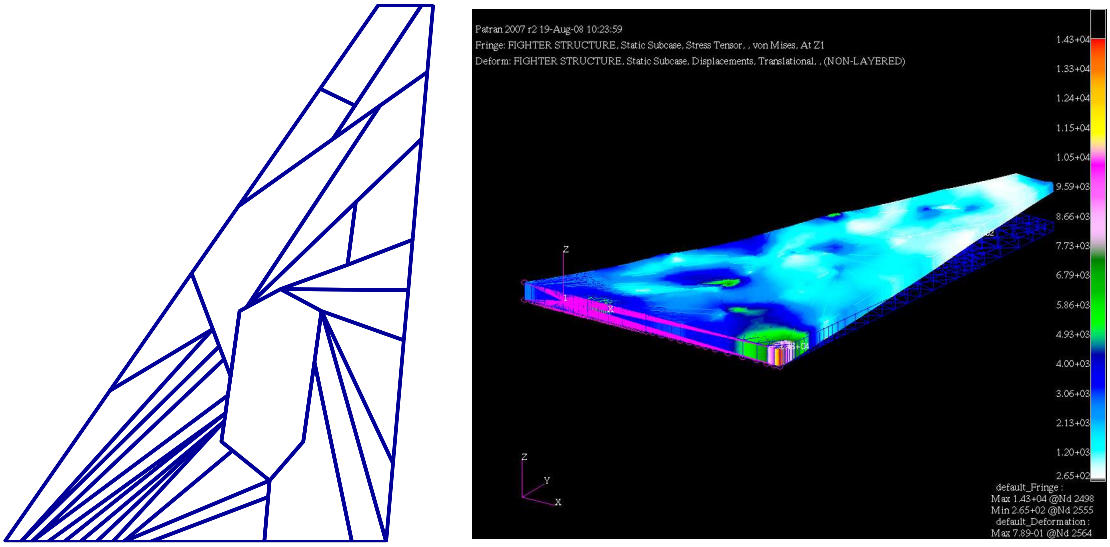

Figure 39: Pareto design: mass = 41.1 %, stress = 20.5 %.

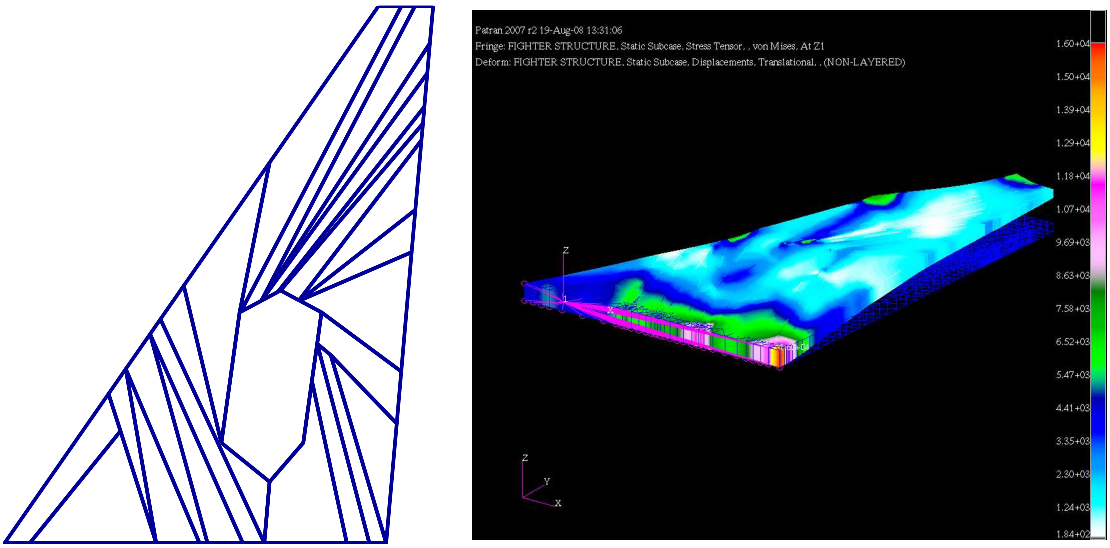

Figure 40: Pareto design: mass = 36.6 %, stress = 27.1 %.

the load among several members.

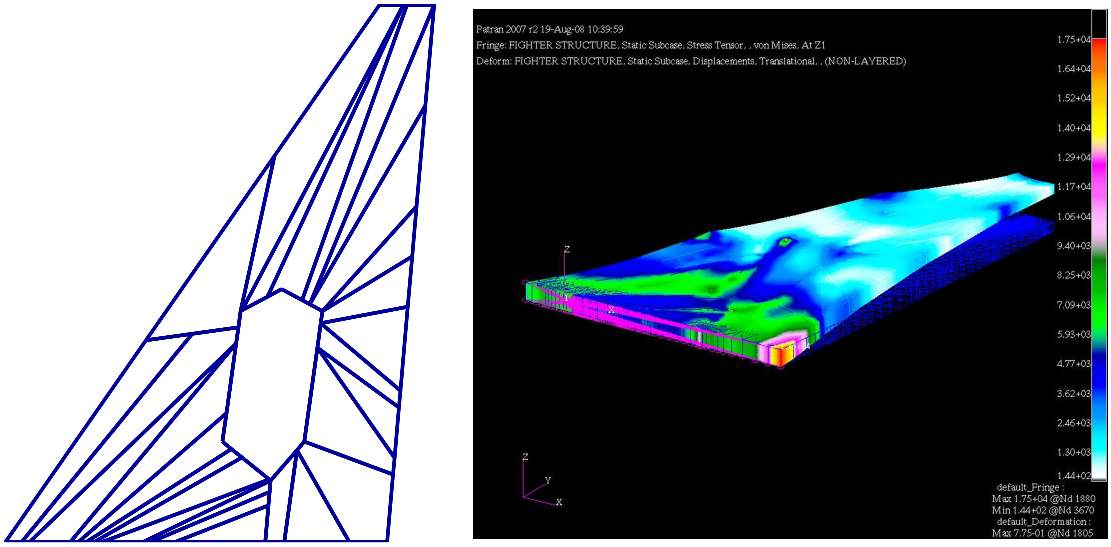

Figure 41: Pareto design: mass = 35.6 %, stress = 28.5 %.

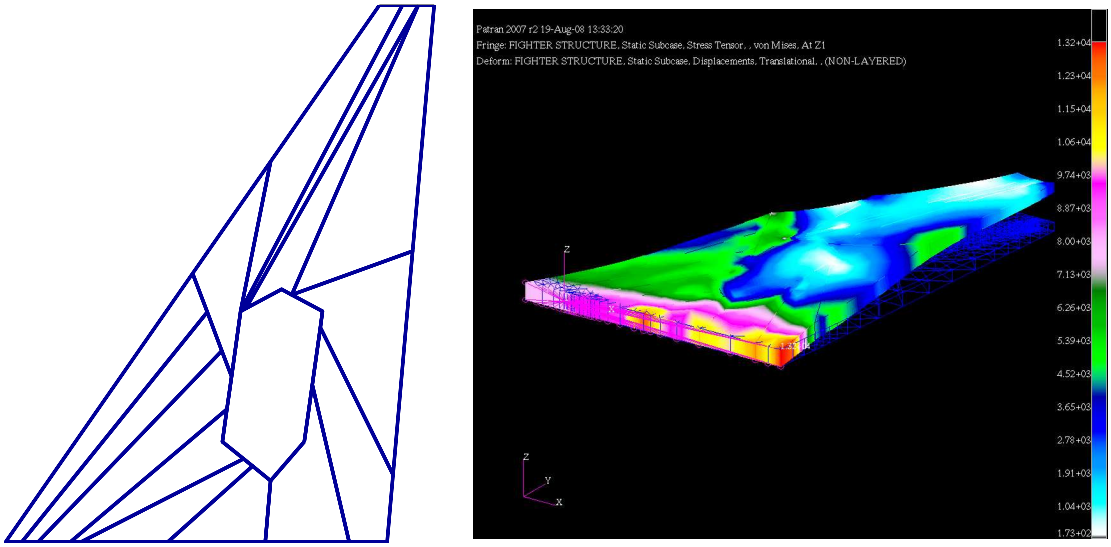

Figure 42: Pareto design: mass = 34.9 %, stress = 35.2 %.

This increased area coverage demonstrates, in passing, the gains of topological optimization when compared to sizing optimization. Indeed, with more mass

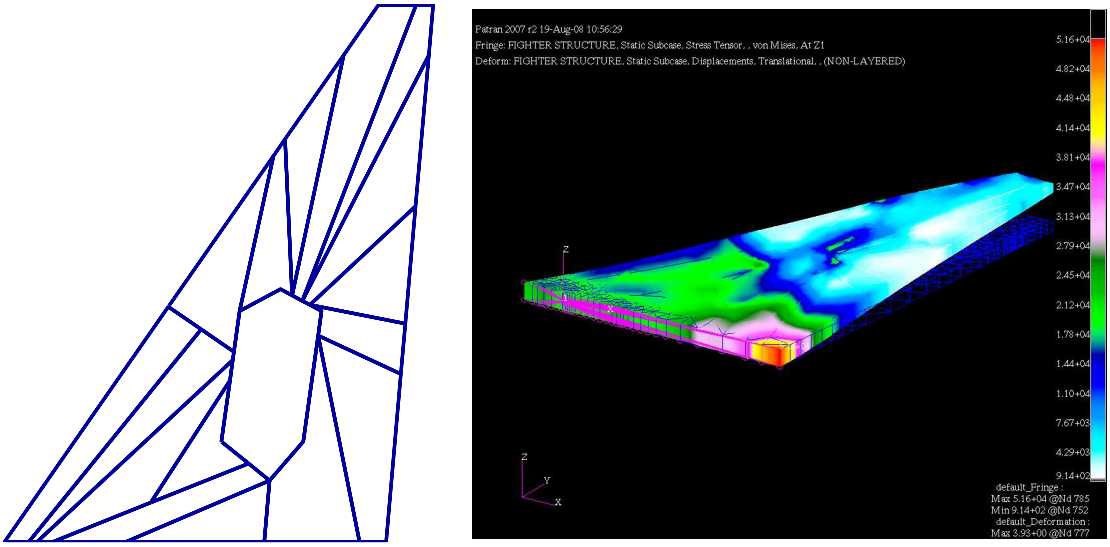

Figure 43: Pareto design: mass = 22.7 %, stress = 43.0 %.

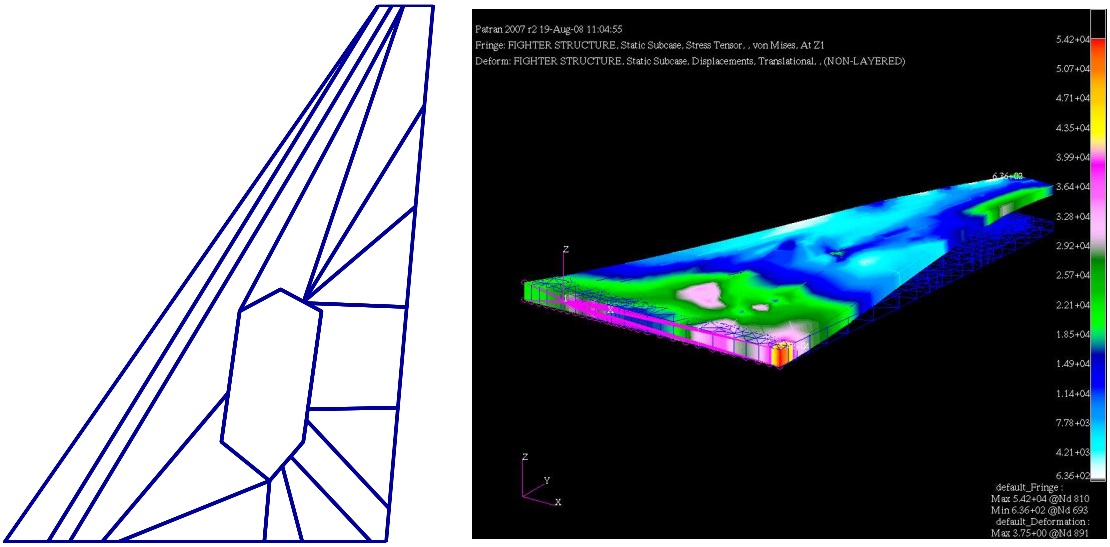

Figure 44: Pareto design: mass = 21.8 %, stress = 58.9 %.

available, it is preferable to redistribute the reinforcements among several shear

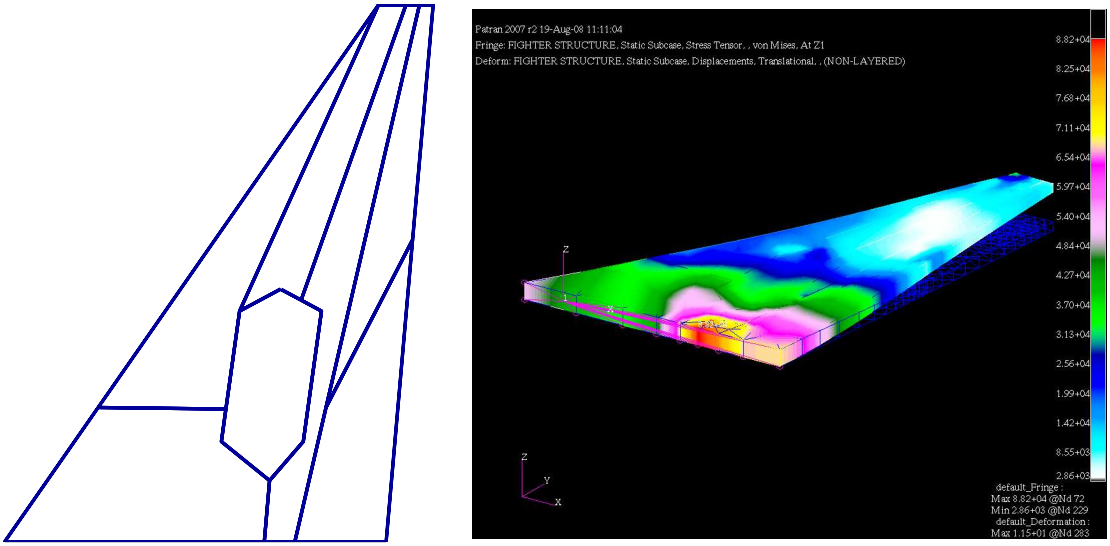

Figure 45: Pareto design: mass = 16.5 %, stress = 82.9 %.

panels rather than increase the thickness of the existing layouts of the low mass designs.

The figures also reveal a larger accumulation of structural reinforcements at the leading-edge section of the wing, specially at the root section. This structural buildup at the leading-edge/root is essential to strengthen the wing against the aerodynamic pressure loads, which peak at the stagnation line close to the leading edge.

4. Satellite adapter

The last test case in this summary, is the design of a structure for a Payload Adapter and Deployer, PAD for short. The PAD's function is to accommodate multiple payloads into the payload bay. In this case the payloads consist in one large satellite, and six small satellites. The PAD with the satellites assembled is shown in figure 46.

Because the highest loads the PAD will experience occur during launching only that stage is considered—after the payloads detached from the PAD its mission has been accomplished and it is discarded. The exact loads experienced by the structure are unknown, thus the conditions for this optimization correspond to a worst case scenario in which the assembled structure—PAD plus the payloads, experiences vertical and lateral accelerations 13 times grater than g.

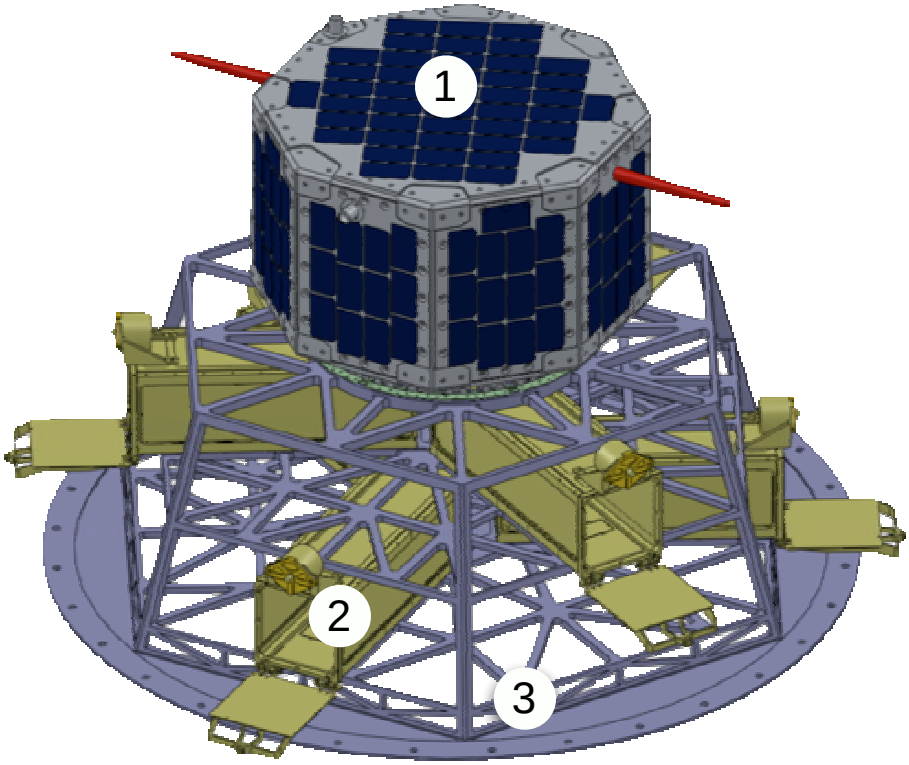

Figure 46: The assembled structure. 1: Large satellite; 2: small satellites; 3: the PAD showing an initial design not optimized.

Figure 46 shows an initial design[2] for the PAD. This design was determined using just the designers experience, and no automatic optimization was performed, apart from sizing by trial and error. This design weights 22 kg and satisfies all the constraints and requirements.

The goal for present optimization is to reduce the mass of the PAD without weakening the structure so that it can withstand the launching phase. For aerospace applications, weight reduction is extremely important for several reasons. In first place, cost reduction as at current prices hauling one kilogram into a low earth orbit cost several thousand dollars. Secondly, the reduction of any unnecessary weight allows for the inclusion of other payloads that can enhance the mission, such as batteries, scientific instruments, etc.

[2]The PIs are grateful to Carol Hude for providing the initial design.

The PAD is built from aerospace aluminum with the following material properties:

Density	2800 kg/m^3
Young's Modulus	71 GPa
Yield stress	572 MPa

Table 4: Material properties

There are several elements of the design are determined a priori . For example, due to payload bay space constraints the geometric envelop for the PAD is well defined—see figure 47. Also the positions of certain elements are constrained such that the satellites can be attached to the PAD. These elements are shown in figure 47 and are designated hereafter as the PAD's "bare bones".

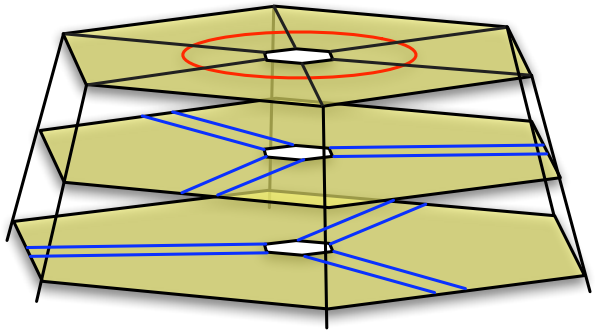

Figure 47: The bare bones of the PAD. The elements onto which the satellites will be attached are highlighted in color, red: large satellite, blue: six small satellites.

The large void areas in the three platforms (highlighted in yellow in figure 47) are free to be "filled" with topologies produced by the Map L-system. The optimization searches for the best structure generated by the PAD's bare bones and Map L-system. Furthermore, the thickness of every beam in the structure is also a optimization variable.

Other than these geometrical constraints that can be easily fulfilled during the geometry modeling, there are maximum stress and maximum displacement constraints. The former must be satisfied to guarantee that the structure does not fail—the latter assures that the deformed PAD will not interfere with the small

satellites and possibly damage them, given that upon assembling gaps between PAD and satellite are narrow. Formally, this problem can be stated as:

$$\begin{array}{rl} \text{minimize} & W(\mathbf{x}) \\ \text{such that} & \sigma_{max}(\mathbf{x}) - \sigma_{lim} \leq 0 \\ \text{and} & \delta_{max}(\mathbf{x}) - \delta_{lim} \leq 0 \end{array} \tag{21}$$

where $W(\mathbf{x})$ is the PAD's weight, $\sigma_{max}(\mathbf{x})$ is the maximum stress experienced by the structure, σ_{lim} is maximum allowed stress level, $\delta_{max}(\mathbf{x})$ is the maximum displacement in the structure and δ_{lim} is the maximum allowed displacement. For this problem the maximum allowed values are:

$$\begin{array}{rcl} \sigma_{lim} & = & \dfrac{\sigma_{yield}}{n} \\ \delta_{lim} & = & 2.0\ cm \end{array} \tag{22}$$

where n is a safety factor equal to 1.5, and the σ_{yield} can be found in table 4.

The PAD's structure can be seen as the assembly of many beams of variable thickness. These structures can be modeled accurately with tridimensional finite elements, however mesh generation can be complex and may require supervision precluding the sought after automatization of the calculus of the fitness function. Thus, as in the previous test cases, a simpler and less computational expensive surrogate model is used to determine the fitness value. For the surrogate model all the tridimensional beams are replaced by Euler beams that assume a linear variation of stress in the transversal direction with the maximum stress located at the external faces of the beam. This approximation is valid because all elements in the PAD have a high ratio of length to thickness, and only small deformations are considered. The usage of Euler beams simplifies the mesh generation greatly since all geometric elements become lines, and reduces the solution time enormously. The differences in the thicknesses of the beams are taken in to account trough the area properties - area and area moments of inertia.

5. Map L-system topology

The PAD structure is formed by the PAD's bare bones plus five different topologies determined by the Map L-system which occupy the voided areas in the three platforms. The way the five maps – one for the top platform, and two for each of the other two, are assembled onto the PAD's bare bones is shown in figure 48.

The different Map L-system settings used in the generation of these topologies are listed bellow.

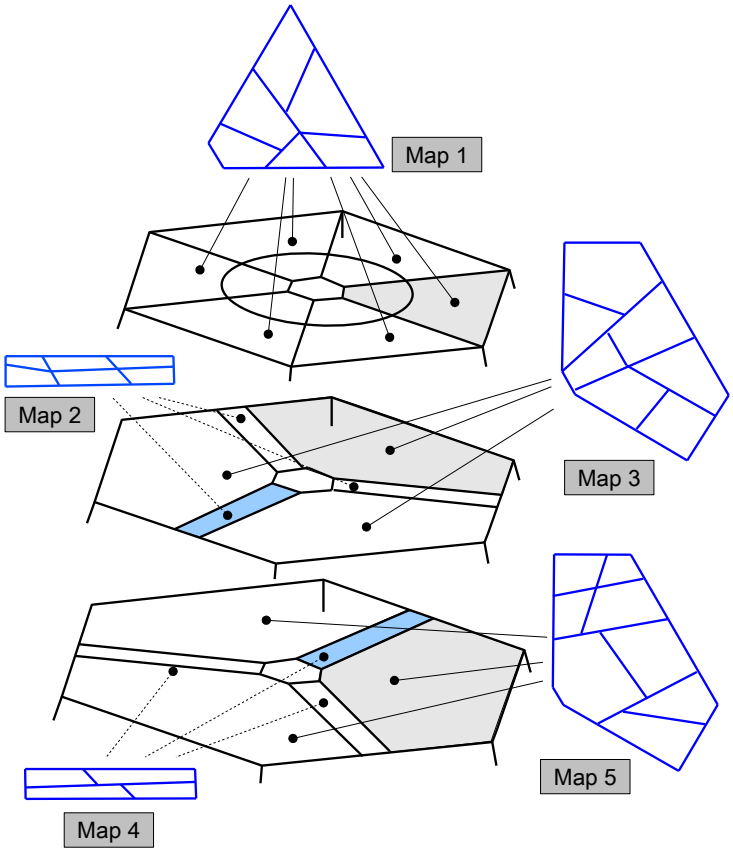

Figure 48: This figure shows how the five different map L-systems are assembled in the PAD bare bones

- Alphabet Σ has 6 letters excluding x.
- The production rules have 6 tokens.
- The number of developmental stages varies between 3 and 6.
- The equilibrium calculation is bypassed.
- Two of the initial maps have 6 edges and the other three have 4 edges. The coordinates of the vertices in the initial maps are such that the Map L-system topology fits in the PAD's bare bones as shown in figure 48.

The PAD must withstand a vertical and lateral acceleration 13 times greater than g with the satellites attached onto it. For simplicity each the satellite is replaced by a lateral and a vertical force of magnitude $13g.m$ where m is the mass of the satellite. The mass of the large satellite is $m_1 = 50\ kg$ and the mass of each one of the small satellites is $m_2 = 5.25\ kg$. These forces are applied to correspondent satellite center of gravity as shown in figure 49. These forces are then transfered to the PAD as distributed forces (force per unit of length) and moments. Furthermore body forces due to the structure's own weight are also considered.

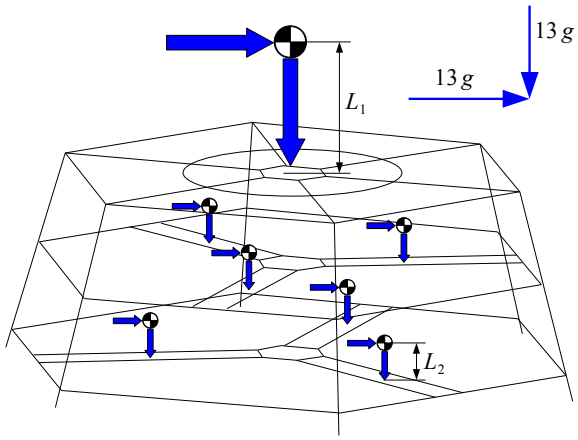

Figure 49: Loads due to the satellites applied at the respective centers of gravity.

The calculation of this forces and moments due to the satellites weight is done in a simple way. For example, all the effects caused by the presence of the large satellite will be transfered to the its attachment points, in this case the ring in the top platform. The vertical acceleration experienced by the satellite causes a distributed load in the vertical direction, whose magnitude is calculated by dividing the satellite's weight at $13g$'s by the perimeter of the ring. As for the lateral acceleration experienced by the satellite its effect is twofold. In first place, it causes a lateral distributed force whose direction is the same as the lateral acceleration and whose magnitude is same as for the vertical force. Secondly, it also provokes a twisting moment on the ring. This moment is simulated by applying a distributed force onto the ring as shown in figure 50. The magnitude of this force is calculated using the schematic in the same figure. The differential torque created by the force distributed over the infinitesimal length $d\theta R$ is $dM = 2FRd\theta Rsin(\theta)$. This can

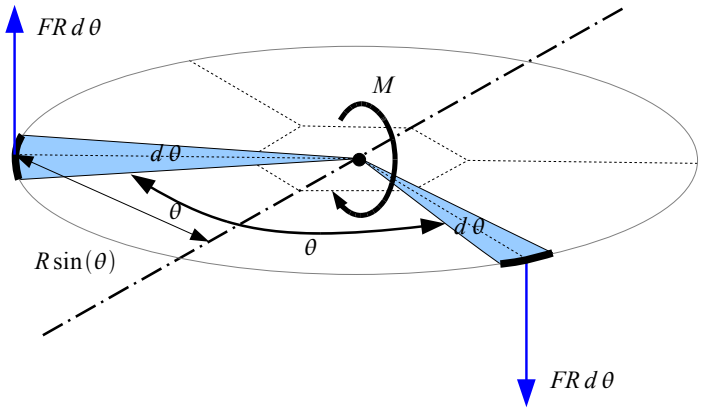

Figure 50: The distributed force F is equivalent to the moment M. R is the radius of the ring to which the large satellite is attached.

be readily integrated for the whole ring and the value of F obtained.

$$M = \int_0^{\pi} 2FR^2 \sin(\theta) d\theta \Rightarrow F = \frac{M}{4R^2} \tag{23}$$

where the moment M is given by $M = 13g \cdot m_1 \cdot L_1$, where L_1 is known. The loads due to the smaller satellites are calculated in a similar manner.

With the tools presented above it is possible to study any PAD design encoded in the vector $\mathbf{x}$. After creating the PAD structure by assembling the PAD's bare bones and the several Map L-system topologies, the tridimensional PAD model is analyzed via the FE method to determine the fitness of the individual. For this weight minimization problem the fitness function is given by:

$$W(\mathbf{x}) + P_\sigma + P_\delta \tag{24}$$

where P_σ and P_δ are the penalization terms for maximum stress and maximum displacement, respectively. These terms are given by:

$$\begin{aligned} P_\sigma &= 5\left(e^{\max(\sigma_{max}-\sigma_{lim},0)} - 1\right) \\ P_\delta &= 5\left(e^{\max(\delta_{max}-\delta_{lim},0)} - 1\right). \end{aligned} \tag{25}$$

With this functional form for the penalization, structures for which the maximum stress and/or maximum displacement are marginally higher than the limiting values are not very penalized.

From the FE method solution the maximum stress and the maximum displacement can be determined. The stresses on the Euler beams results from traction/compression and also from bending. To avoid complicated calculations to determine the actual maximum tension on each beam, a conservative value for the maximum stress in the structure is used:

$$\sigma_{max} = |\sigma_{max,bending}| + |\sigma_{tension}| \tag{26}$$

where the values $\sigma_{max,bending}$, and $\sigma_{tension}$ are readily available in the COMSOL post-processing functions.The maximum displacement in the PAD (δ_{max}) is also calculated with the COMSOL postprocessing functions.

The mass is calculated by integrating the cross-sectional area along the beams length. This calculation yields a conservative value for the PAD's mass since it takes into account the mass in the intersecting beams twice, as exemplified in figure **??**. It is shown ahead this can cause a difference of more than 15% between the mass for the surrogate model and the mass for the real structure.

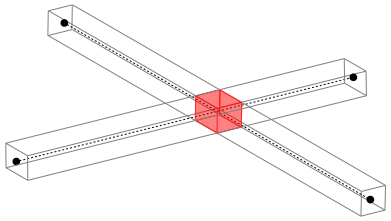

Figure 51: The calculation of the mass is conservative because the mass of the cube highlighted in the intersection of the two beams is counted twice.

The bioTOM settings for the evolutionary algorithm for this single objective optimization are listed below.

- There are 100 individuals per population.
- The initial populations were generated randomly.
- The Genetic Algorithm ran for 100 iterations or until no improvement was observed.
- The new generations were formed by 5% elite individuals, 80% crossover offsprings and 15% mutated individuals.

- The crossover, selection and mutation operators are as explained above.
- The genome is encoded in vector of reals, $\mathbf{Y}$, whose elements are vary between 0 and 1, just as it was described above, but now five different Map L-system must be coded instead of just one plus the thickness for the PAD bare bones elements. Figure 52 the structure of $\mathbf{Y}$.

Figure 52: The genome codification for the PAD.

The convergence history for the best design is depicted in figure 53.

As expected the curve flattens out as the "best" information in the genetic pool becomes concentrated in one individual. After 70 generations only very small improvements are observed from generation to generation.

Figure 53 also depicts the platforms structures for the best individuals in intermediate generations. An important conclusion for this particular case, and perhaps a conclusion that goes against initial conceptions, is that the best structure is a rather simple one. One can see from these figures a constant reduction of the number of beam elements for the best structure as the number of generations increases, and at the same time the fine tuning of the beams thickness. Figure 54 shows the beams thicknesses for the same individuals as in the inserts in figure 53.

The optimal structure after the 100 generations is depicted in figure 55. The relevant variables for this individual are listed below:

- the mass, $mass_{PAD} = 15.4\ kg$, which represents a reduction of 30% in the mass of the structure when compared to the initial design (22 kg);
- the maximum stress, $\sigma_{max} = 294\ MPa$ is below the 300 MPa as required;
- and finally the maximum displacement, $\delta_{max} = 1.6$ cm, is also below the limiting value of 2 cm.

In order to validate this results the optimal design was modeled in a more realistic manner. The beams were modeled as tridimensional solid elements and the satellites were included in the model to simulate the loads applied to the PAD

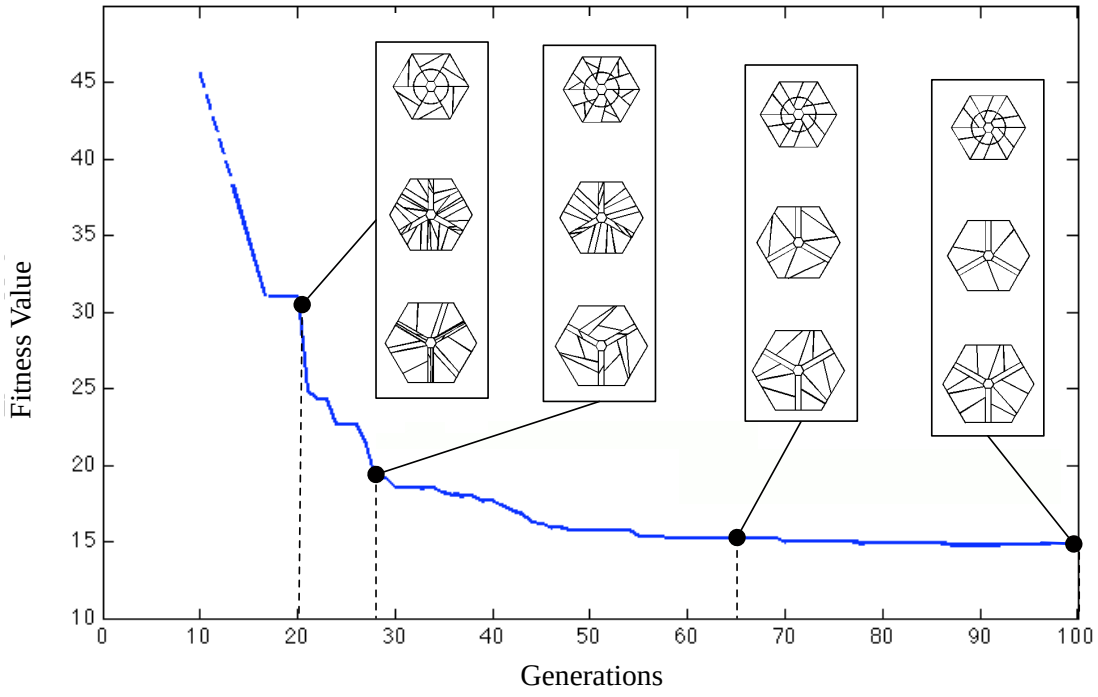

Figure 53: Evolution of the best PAD design. The inserts depict the structure of the platforms for some selected individuals, all of them the best of their respective generation.

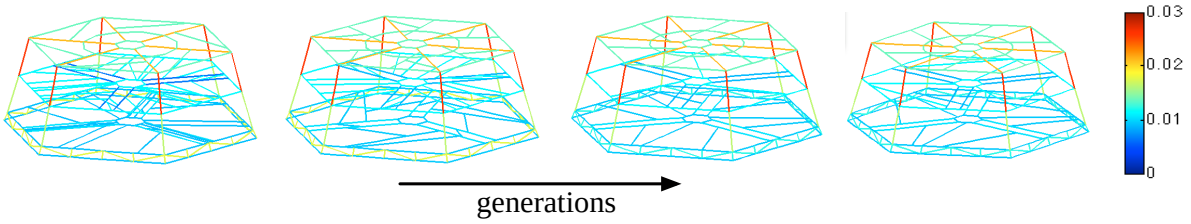

Figure 54: The thickness of the beams for the same individuals as in figure 53. The color represents the thickness value in meters.

more accurately. The satellites are assumed to be rigid and homogeneous masses with dimensions such that their centers of gravity correspond to the ones from real

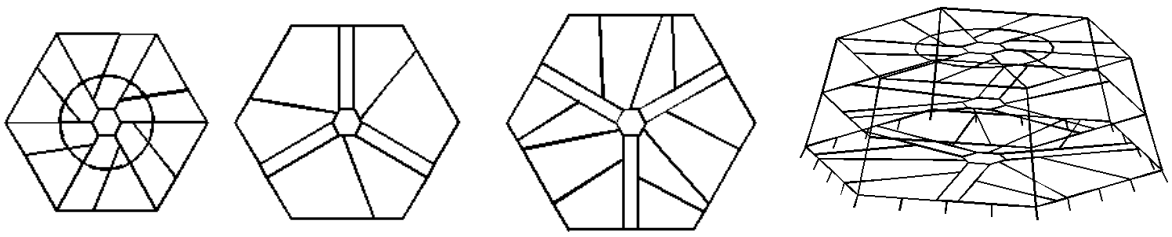

Figure 55: The structure of the 3 platforms for the best individual after 100 generations, and the assembled geometry. (a) top platform, (b) middle platform, (c) bottom platform and (d) assembled structure.

satellites. The simulated geometry is depicted in figure 56.

The stresses and the displacements are is shown in figure 58. In this case the Von Mises stresses were used as the failure criterion. The results show some differences with respect to the surrogate model but in general the agreement in the maximum values for stress and displacement and the location in the structure where they occur is satisfactory, as seen in figures 58 and 57. Furthermore, the realistic model also satisfies all the displacement and stress constraints. As for the mass, and because of the reasons pointed above, its value decreased to 13 kg, which represents a mass reduction of 41% from the initial design.

To finalize the PAD was redesigned[3] in detail following what was learned from the bioTOM. The final design for the PAD is shown in figure 59. In the end the mass of the structure increased slightly to 13 kg however that still represents a remarkable decrease of 41% in the mass with respect to the initial design.

§3. MAIN FINDINGS

In this work, a novel paradigm for aerospace structural-topology design was introduced and assessed. This paradigm is inspired on the cellular division of living organisms, which, similarly to engineering design, depends on their fitness to survive or replicate. The following is a summary of the main findings of this research:

[3]The author thanks again to Carol Hude for providing the final design.

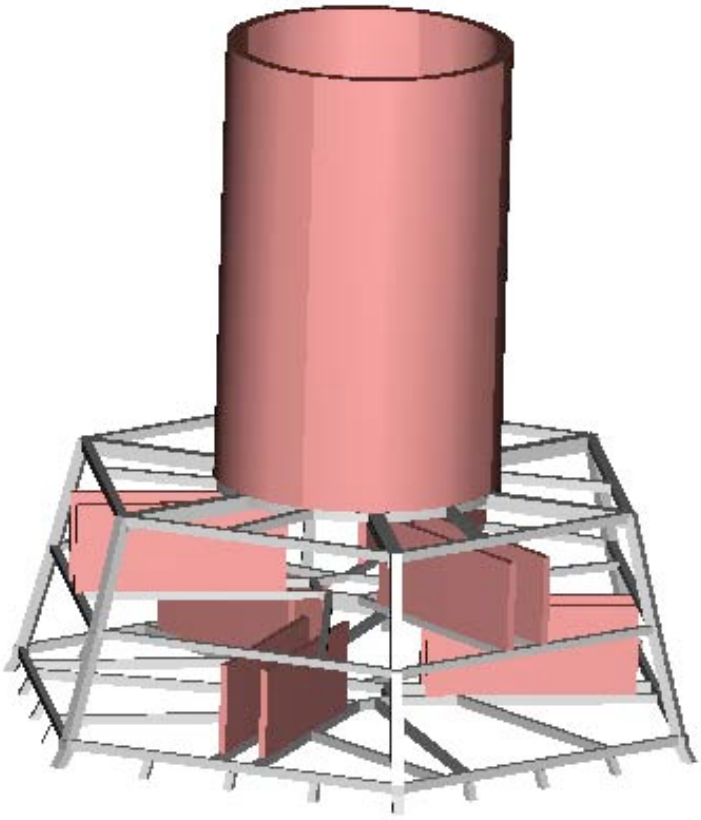

Figure 56: The tridimensional PAD structure with the satellites assembled.

1. bioTOM evolves engineering designs that are higher-performing than the designs obtained with Genetic Algorithm. In test cases carried-out comparing the proposed bioTOM and Genetic Algorithm, bioTOM consistently evolved higher-performing designs. The main reasons for this improved design are twofold: (a) the evolution-development (EvoDevo) paradigm, and (b) bioTOM generates a much larger proportion of feasible designs. The import of EvoDevo paradigm derives from mainly for two reasons, it provides a more effective searching of the design space and it provides designs with better resolution. The former advantage can be easily grasped in the biological context, which inspired bioTOM. Indeed, a mutation of a single cell would provide exceedingly small variation in the design to be an effective agent of change in the individual fitness (unless, that is, the design is so unstable that a vanish-

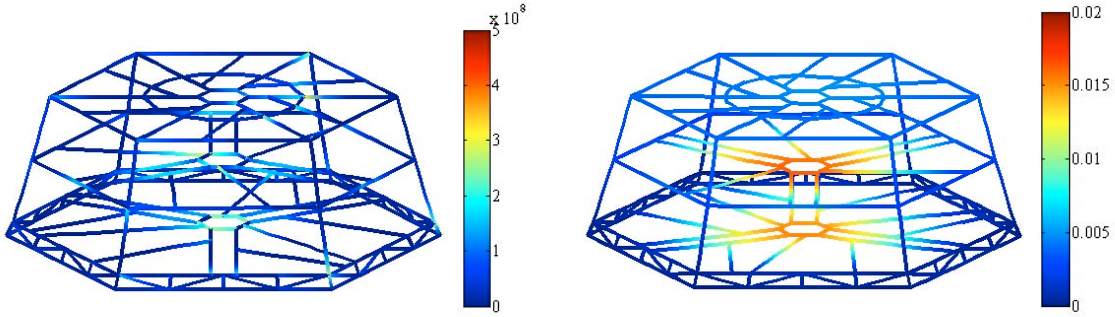

(a) (b)

Figure 57: The finite element solution simplified (Euler beams) model of the PAD. (a) Stresses [Pa] calculated using equation 26, (b) the deformed structure [m].

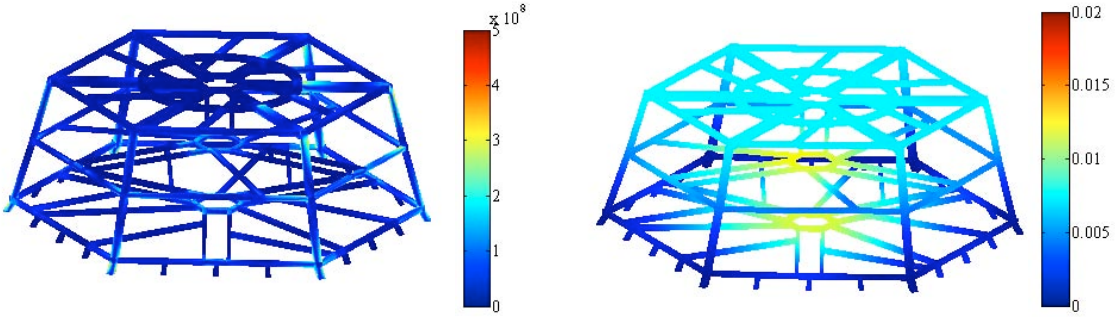

(a) (b)

Figure 58: The finite element solution for the tridimensional model of the PAD. (a) The Von Mises stresses [PA], (b) the deformed structure [m]

ingly small variation in its phenotype would lead to large variation in the its associated fitness; a prospect that would be arguably of any use either in biology or engineering.) The second advantage of EvoDevo allows for a more effective search of the design space by providing fincreased definition with smaller genes. A smaller gene in its turn allows for a more efficient search of the design space. The other main advantage of bioTOM over Genetic Algorithm is the fact that a much larger fraction of the population in each generation is feasible (test case 1). One reason for that stems from the network structure intrinsic to bioTOM but which has to be "learned" by

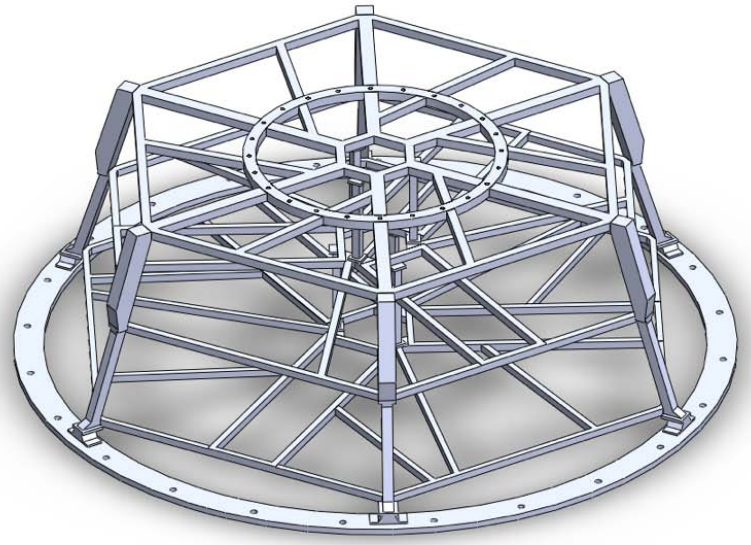

Figure 59: The optimized PAD structure.

trial-and-error in the conventional Genetic Algorithm.

2. bioTOM evolves better designs than Genetic Algorithm in a fraction of the number of generations needed by Genetic Algorithm. This advantage follows from the more effective search of the design space explained above using bioTOM as compared with the Genetic Algorithm. Because this search is substantially better that the conventional search with Genetic Algorithm, bioTOM can obtain higher performing designs than Genetic Algorithm in one order of magnitude less generations than Genetic Algorithm.

3. bioTOM evolves better designs than Genetic Algorithm using a fraction of the number of genes needed by Genetic Algorithm. Again, this is a consequence of EvoDevo model used in bioTOM. Indeed, the number of genes in living organisms is only a minute fraction of the number of cells they regulate. Thus the fact that the DNA encodes a program that develops organisms, engenders a diversity of effective solutions that can be found and evolved in a timely manner. This advantage was shown in this research to be equally relevant in searching for optimal engineering designs as well.

4. bioTOM evolves designs that are as high-performing as SIMP, when the conditions suit SIMP, but provide better designs than SIMP overall. If a problem is well posed, the sensitivity bounded and smooth, the fitness landscape convex and the optimal topology relatively simple, then SIMP will converge to the optimal design as the mesh is refined. The problem is that these conditions are seldom met in real applications—they are not met even in the simplest of the test cases above. It is nonetheless reassuring that bioTOM will generate solutions that perform as well as SIMP when the conditions are propitious for SIMP (test case 2). Overall, bioTOM will perform better because of the increased resolution of the topology as explained above and because it searches for global minima, instead of local minima as in SIMP.

5. bioTOM is more versatile than SIMP. As mentioned in the previous item, SIMP requires a number of conditions for its adequate use. Because bioTOM do not require these same conditions, it can be applied to a more varied class of problems as compared to SIMP. For instance, bioTOM does not require the *a priori* definition of the region, called design domain, over which the design is sought, bioTOM does not require a regular fitness function or constraint, a maximum stress is a case in point, bioTOM does not simulate empty space, and bioTOM searches for global minima, instead of local minima in SIMP. The latter is particularly relevant for engineering applications, where the complexity and non-linearity of the constraints and objective functions lend themselves to multi-minima problems. In these cases, the solution using SIMP would greatly depend on the initial condition.

6. bioTOM is more easily integrates existing COTS software. In this research, bioTOM was easily integrated with three different software: COMSOL, NASTRAN and a in-house vortex lattice method code. By contrast, SIMP requires the computation of sensitivities and these computations are not easily implemented in COTS codes. For instance, these calculations could be implemented using a general finite-differences approach. In this case, the price of generality would be poor performance at best and inaccurate and diverging sequences of designs at worst. Alternatively, specific and exact gradient calculation could be sought. However, such approach would be hardly integrable with existing software, as it would require programing the sensitivities for each objective function and for each different application. That could only e accomplished with access to the source code of the COTS software—a virtual impossibility in most cases.

7. bioTOM provides better solutions for engineering design than conventional biomimetics. Instead of mimicking extant biological structures for engineering design, as in biomimetic approaches, the proposed methodology seek to model and simulate the EvoDevo mechanisms that led to the emergence of those structures in the first place. This distinction is critical for engineering design because the requirements, constraints and material available for living organisms are utterly distinct from engineering design. And because there are some applications for which no biological model exists, spacecraft design is a case in point.

Although more studies are required to further validate and refine the methodology, the results reported in this work clearly demonstrate that, with expected extensions and improvements, the methodology can play a key role in the design of novel and better performing aerospacel structures. In fact, no one doubts the prime role of EvoDevo in the evolution of the species. This research showed that synthetic EvoDevo can be as consequential and beneficial for engineering design as biological EvoDevo is for the evolution of natural organisms.

§4. PERSONNEL SUPPORTED

The grant supported the following personnel:

Faculty

1. Marcelo H. Kobayashi, PI, Professor of Mechanical Engineering, University of Hawaii at Manoa.

2. Marguerite A. Butler, Co-PI, Assistant Professor of Zoology, University of Hawaii at Manoa.

3. Alexandre K. da Silva, Co-PI, Assistant Professor of Mechanical Engineering, University of Hawaii at Manoa (currently at The University of Texas at Austin).

Graduate Students

4. Hugo-Tiago C. Pedro, Ph. D., University of Hawaii at Manoa, defense scheduled to April 28, 2010, "Biologically Inspired Design"[4], advisor: M.H.

[4]Requests for Ph.D. dissertations or M.Sc. theses should be directed to the Graduate Division of the University of Hawaii at Manoa: http://www.hawaii.edu/graduate/organization/html/admin.htm

Kobayashi.

5. Kim Wai Leung, M.Sc., University of Hawaii at Manoa, "Computational Study of Insect Wing", Summer 2009, advisor: M.H. Kobayashi.

6. Alexander T. Le Bon, M.Sc., University of Hawaii at Manoa, defense scheduled for May 3, 2010, "On a Biologically Inspired Method for Shape and Topology Optimization of Aircraft Wings", advisor: M.H. Kobayashi.

Post Doctoral Fellow

7. J. Walguarnery, Department of Zoology, advisor: M. A. Butler.

In addition to the students supported by the grant, the following students have collaborated in the project at no cost:

Graduate Students

1. E. Sabbatini, M.Sc., international exchange student from *Università Politecnica delle Marche - Ancona*, Italy, "Theoretical and Experimental Study of New Methods for Biologically Inspired Optimization of Structures, Application to a Vibration Suppression Problem", UH advisor: M.H. Kobayashi.

2. M.A. Nunes, M.Sc., University of Hawaii at Manoa, "A Biologically Inspired Methodology for Aerospace Vehicles Design", expected Summer 2010, advisor: M.H. Kobayashi. Support from LEONIDAS project—see below.

NASA Grant fellow

3. K. Sexton, "Bio-inspired Design of Thermal Systems for Small Satellites". Mr. Sexton is currently a graduate student at Dartmouth University.

§5. PUBLICATIONS

The following publications acknowledge the support of this grant:

Journal

1. M. H. Kobayashi, H-T. C. Pedro, R.M. Kolonay and G.W. Reich (2009) On a Cellular Division Method for Aircraft Structural Design, The Aeronautical Journal of the Royal Aeronautical Society (113) 821–831.

2. M.H. Kobayashi (2010) On a Biologically Inspired Topology Optimization Method, Communications in Nonlinear Sciences and Numerical Simulations (15) 787—802.

3. M.H. Kobayashi, H-T. C. Pedro, C. F. M. Coimbra and A.K. da Silva (2009) Formal Evolutionary Development of Low-Entropy Dendritic Thermal Systems AIAA Journal of Thermophysics and Heat Transfer (23) 822–827.

4. H. Pedro, M. H. Kobayashi, C. F. M. Coimbra and A. K. da Silva, Effectiveness of Complex Design Through an Evolutionary Approach, Journal of Thermophysics and Heat Transfer 22 (2008) 115–118.

Conference

5. M.H. Kobayashi, R.M. Kolonay, G. W. Reich, A. LeBon, H-T.C. Pedro (2010) On a Cellular Division Model for Multi-Disciplinary Optimization, 51st AIAA/ASME/ASCE/AHS/ASC Structures, Structural Dynamics, and Materials Conference in Orlando, Florida.

6. M. H. Kobayashi, H-T. C. Pedro, R.M. Kolonay and G.W. Reich (2009) "On a Cellular Division Method for Topology Optimization", 50th AIAA/ ASME/ASCE/AHS/ASC Structures, Structural Dynamics, and Materials Conference, Palm Springs, California.

7. H.T.C. Pedro and M.H. Kobayashi (2009) Optimization of cellular structures using map L-systems, 47th AIAA Aerospace Sciences Meeting and Exhibit Orlando, Florida.

8. E. Sabbatinii, G.-M. Revel, M.H. Kobayashi (2009) On a biologically inspired topology optimization method for vibration suppression, 47th AIAA Aerospace Sciences Meeting and Exhibit Orlando, Florida.

9. M. H. Kobayashi, H. T. C. Pedro, C. F. M. Coimbra and A.K. da Silva (2008) The Formal Evolutionary Development of Low Entropy Dendritic Thermal, 11th IEEE International Conference on Computational Science and Engineering (CSE-08), paper SEC08-194, So Paulo, Brazil.

10. H. T. C. Pedro and M. H. Kobayashi (2008) Optimization of Cellular Structures Using Map L Systems 49th AIAA/ASME/ASCE/AHS/ASC Structures, Structural Dynamics, and Materials Conference, paper AIAA-2008-2303, Schaumburg, IL.

§6. INTERACTIONS

In the period of this grant, the following interactions have taken place:

1. DURIP 08 - Instrumentation of Fabrication, Characterization and Experimental Validation of Micro Aerial Vehicles with Flexible Wings based on Evolutionary Aeroelastic Optimization. P.I. Jian-Qiao Sun Professor, School of Engineering, University of California, Merced. Award amount: $\$500,000$. The experimental setup started operation in December 2009 at the University of California, Merced. M.H. Kobayashi is a Co-PI in this project and its purpose is to fabricate and test the biologically inspired designs generated by bioTOM.

2. NATO-RTO Characterization of Bio-Inspired Micro Air Vehicle Dynamics. Chair: Dr. Philip S. Beran, AFRL/WP. Lead Nation: United States. Participating nations: CAN, FRA, DEU, NLD, NOR, POL, PRT, TUR, GBR & USA. The RTO is tasked to foster the technical strength of the member nations. The proposed subject matter directly addresses NATO security needs for unconventional threat environments. To expand capability for intelligence, surveillance, and reconnaissance (ISR) in military operations, much attention has recently been given to the operational potential of micro air vehicles. This project addresses vehicles whose propulsion is produced by moving wings, e.g., inspired by bird, bat, and insect flight. M.H. Kobayashi is a member of this project and his task is to use bioTOM to design novel, biologically inspired MAVs with expanded capability for ISR missions. This interaction allowed M.H. Kobayashi to initiate a collaboration with Dr. Beran, and a part of that collaboration Dr. Stanford, who is a post-doctaral fellow advised by Dr. Beran, kindly offered his SIMP code for comparison. The code for bioTOM developed here was also exchanged with Dr. Stanford as part of this collaboration.

3. Low Earth Orbit Nanosat-Integrated Defense Autonomous System. Director: Luke Flynn, Researcher at School of Ocean and Earth Science and Technology at the University of Hawaii at Manoa. The goal of this project is to develop, for the first time in a single institution, the infrastructure and personnel needed to design, fabricate and lunch small satellites. M.H. Kobayashi is the leader of the Thermal Control Subsystem and also participates in the design of the spectrometer box and satellite structure for the HawaiiSat satellite—currently under development within LEONIDAS. In this work, we plan to pioneer the use of topology optimization in the development of light, high-performing structures for the satellite bus and payload..

4. American Society for Engineering Education Fellow at Wright-Patterson Air Force Research Laboratory 2009 Air Force Summer Faculty Fellowship Program. M. H. Kobayashi was a fellow at AFRL/WP during the summer of 2009. The scientific advisors for this fellowship were Dr. Raymond M. Kolonay and Dr. Gregory W. Reich, both at AFLR/WP. In this interaction, the shape and topology optimization of an MAV was carried-out. The results of this interaction will be presented at the 51st AIAA/ASME/ASCE/AHS/ASC Structures, Structural Dynamics, and Materials Conference in Orlando, Florida. Graduate student A.T LeBon was also a fellow with M. H. Kobayashi at AFRL/WP during the summer of 2009. During this fellowship, Dr. Kolonay and M. H. Kobayashi prepared the draft of a successful grant with AFOSR in the area of Structural Mechanics. This interaction also provided an opportunity for M.H. Kobayashi to acquaint himself with NASTRAN.

5. Air Force Research Laboratory/Air Vehicles Directorate (AFRL/RB) 2008 Summer Researcher Program Fellowship. M. H. Kobayashi was a fellow at AFRL/WP during the summer of 2008. In this interaction, two research projects were planned and executed. The first project aimed at optimizing the mechanism for a morphing wing technology. The mechanism was design and the results were published as an AIAA paper for the 50th AIAA/ ASME/ASCE/AHS/ASC Structures, Structural Dynamics, and Materials Conference, Palm Springs, California. The second project investigated the optimal design for the wing box of a generic fighter. The results of this research were published in The Aeronautical Journal of the Royal Aeronautical Society.

6. Class on Comparative Biomechanics. Another important interaction during this period was the development and teaching of a new technical elective course on Comparative Biomechanics for students of both Biology and Engineering Majors. The course was jointly developed by M. H. Kobayashi and M. A. Butler, and was well received by the students, with fourteen engineering students and three biology students enrolling in the class—this enrollment is more than double the number of students that regularly enroll in technical elective classes in engineering.

§7. NEW DISCOVERIES, INVENTIONS OR PATENT DISCLOSURES

Provisional patent 61/284,520 on bioTOM.

§8. HONORS/AWARDS

1. American Society for Engineering Education Fellow at Wright-Patterson Air Force Research Laboratory 2009 Air Force Summer Faculty Fellowship Program.

2. Air Force Research Laboratory/Air Vehicles Directorate (AFRL/RB) 2008 Summer Researcher Program Fellowship.

REFERENCES

[1] Dawkins, R., *The Oxford Book of Modern Science Writing*, Oxford University Press, Oxford, UK, 2008.

[2] Prusinkiewicz, P. and Lindenmayer, A., *The Algorithmic Beauty of Plants*, Springer Verlag, New York, 2004.

[3] Lindenmayer, A., "Mathematical Models for Cellular Interactions in Development I. Filaments with One-Sided Inputs," *Journal of Theoretical Biology*, Vol. 18, 1968, pp. 280—299.

[4] Lindenmayer, A., "Mathematical Models for Cellular Interactions in Development II. Simple and Branching Flaments with Two-Sided Inputs," *Journal of Theoretical Biology*, Vol. 18, 1968, pp. 300—315.

[5] Rozenberg, G. and Salomaa, A., *Handbook of Formal Languages*, Springer Verlag, 1997.

[6] Lindenmayer, A. and Rozenberg, G., *Graph Grammars and Their Applications to Computer Science*, chap. Parallel Generation of Maps: Developmental Systems for Cell Layers, Lecture Notes in Computer Science, Springer, Berln, 1979, pp. 301—316.

[7] Nakamura, A., Lindenmayer, A., and Aizawa, K., *The Book of L*, chap. Some Systems for Map Generation, Springer, Berln, 1986, pp. 323—332.

[8] Tutte, W. T., *Graph Theory*, Addison-Wesly, Reading, Massachusetts, 1982.

[9] Goldberg, D. E., *Genetic Algorithms in Search, Optimization, and Machine Learning*, Addison-Wesley, 1989.

[10] Sarker, R., Mohammadian, M., and Yao, X., editors, *Evolutionary Optimization*, Kluwer Academic Publishers, Dordrecht, The Netherlands, 2002.

[11] Coello, C. A. C., *Evolutionary Optimization*, chap. Evolutionary Multi-Objective Optimization: a Critical Review, Kluwer, Secaucus, 2002, pp. 117—146.

[12] Deb, K., *Multi-Objective Optimization using Evolutionary Algorithms*, John Wiley & Sons, Ltd, Chichester, UK, 2001.

[13] ad Fran¸ois Jouve, H. H., Lutton, E., Schoenauer, M., and Sebag, M., "Compact Unstructured Representations for Evolutionary Design," *Applied Intelligence*, Vol. 16, No. 2, 2002, pp. 139—155.

[14] Wang, S. Y. and Tai, K., "Structural topology design optimization using Genetic Algorithms with a bit-array representation," *Computer Methods for Applied Mechanics and Engineering*, Vol. 194, No. 36–38, 2005, pp. 3749—3770.

[15] Balamurugan, R., Ramakrishnan, C., and Singh, N., "Performance evaluation of a two stage adaptive genetic algorithm (TSAGA) in structural topology optimization," *Applied Soft Computing*, Vol. 8, No. 4, 2008, pp. 1607—1624.

[16] Stanford, B. and Ifju, P., "Aeroelastic topology optimization of membrane structures for micro air vehicles," *Structural and Multidisciplinary Optimization*, Vol. 38, No. 3, 2009, pp. 301—316.

[17] Katz, J. and Plotkin, A., *Low-Speed Aerodynamics*, Cambridge University Press, Cambridge, UK, 2001.

[18] Bendsøe, M. P. and Sigmund, O., *Topology Optimization: Theory, Methods and Applications*, Springer, New York, 2nd ed., 2003.

[19] Ern, A. and Guermond, J.-L., *Theory and Practice of Finite Elements*, Springer Verlag, Berlin, D, 2004.

[20] Zienkiewicz, O. C., Taylor, R. L., and Zhu, J. Z., *The Finite Element Method: Its Basis and Fundamentals*, Elsevier Butterworth-Heinemann, sixth ed., 2005.

[21] Zienkiewicz, O. C. and Taylor, R. L., *The Finite Element Method: For Solid and Structural Mechanics*, Elsevier Butterworth-Heinemann, sixth ed., 2005.

[22] Albano, E. and Rodden, W. P., "A Doublet-Latice Method for Calculating Lift Distributions on OScillating Surfaces in Subsonic Flows," *AIAA Journal*, Vol. 7, 1969, pp. 279—285.

[23] Giesing, J. P., Kalman, T. P., and Rodden, W. P., "Subsonic Steady and Oscillatory Aerodynamics for Multiple Interfering Wings and Bodies," *Journal of Aircraft*, Vol. 9, 1972, pp. 693—703.